



Complete characterization of the 3p Rydberg complex of a molecular ion: MgAr⁺

I. Observation of the Mg(3pσ)Ar⁺ B⁺ state and determination of its structure and dynamics

Journal Article

Author(s):

Wehrli, Dominik; Génévriez, Matthieu; [Knecht, Stefan](#) ; [Reiher, Markus](#) ; Merkt, Frédéric

Publication date:

2020

Permanent link:

<https://doi.org/10.3929/ethz-b-000432213>

Rights / license:

[In Copyright - Non-Commercial Use Permitted](#)

Originally published in:

The Journal of Chemical Physics 153(7), <https://doi.org/10.1063/5.0015603>

Funding acknowledgement:

172620 - Precision measurements with cold molecules: Rydberg states, ions and photoionization (SNF)
743121 - Cold Ion Chemistry - Experiments within a Rydberg Orbit (EC)

1 **Complete characterization of the 3p Rydberg complex of a molecular ion: MgAr⁺**
2 **I. Observation of the Mg(3p_σ)Ar⁺ B⁺ state and determination of its structure and**
3 **dynamics**

4 Dominik Wehrli,¹ Matthieu Génévriez,¹ Stefan Knecht,¹ Markus Reiher,¹ and Frédéric
5 Merkt^{1, a)}
6 *Laboratory of Physical Chemistry, ETH Zurich, CH-8093 Zurich,*
7 *Switzerland*

We report on the experimental observation of the B⁺ 2Σ⁺ state of MgAr⁺ located below the Mg⁺(3p 2P_{3/2}) + Ar(1S₀) dissociation asymptote. Using the technique of isolated-core multiphoton Rydberg-dissociation spectroscopy, we have recorded rotationally resolved spectra of the B⁺ 2Σ⁺(v') ← X⁺ 2Σ⁺(v'' = 7) transitions which extend from the vibrational ground state (v' = 0) to the dissociation continuum above the Mg⁺(3p 2P_{3/2}) + Ar(1S₀) dissociation threshold. The analysis of the rotational structure reveals a transition from Hund's angular-momentum-coupling case (b) at low v' values to case (c) at high v' values caused by the spin-orbit interaction. Measurements of the kinetic-energy release and the angular distribution of the Mg⁺ fragments detected in the experiments enabled the characterization of the dissociation mechanisms. The vibrational levels of the B⁺ state above v' = 6 are subject to pre-dissociation into the Mg⁺(3p 2P_{1/2}) + Ar(1S₀) continuum and the fragment angular distributions exhibit anisotropy β parameters around 0.5, whereas direct dissociation into the continuum above the Mg⁺(3p 2P_{3/2}) + Ar(1S₀) asymptote is characterized by β parameters approaching 2. Molecular ions excited to the B⁺ state with v' = 0 – 6 efficiently absorb a second photon to the repulsive part of the 2Σ⁺ state associated with the Mg⁺(3d 2D_{3/2,5/2}) + Ar(1S₀) continua. The interpretation of the data is validated by the results of *ab initio* calculations of the low-lying electronic states of MgAr⁺, which provided initial evidence for the existence of bound vibrational levels of the B⁺ state and for the photodissociation mechanisms of its low vibrational levels.

^{a)}merkt@phys.chem.ethz.ch

8 I. INTRODUCTION

9 The ground electronic states of a large number of small molecular cations have been
10 characterized following the development of ion-beam and ion-spectroscopy techniques¹⁻¹⁰.
11 Data concerning their electronically excited states are, however, much scarcer, in particular
12 concerning their Rydberg states, the behavior of which is by far not as well understood as
13 in the case of neutral molecules.

14 Rydberg states of neutral molecules can be described, in first approximation, as consisting
15 of a molecular ion core in a given rovibronic state and a weakly bound Rydberg electron
16 moving in a distant hydrogen-like $n\ell m_\ell$ orbit. The potential-energy functions of Rydberg
17 states thus resemble those of the corresponding ion-core electronic state. The interaction
18 between the Rydberg electron and the ion core rapidly decreases with increasing n and ℓ
19 values, so that decay by predissociation and autoionization is suppressed at high n or ℓ values.
20 The ground electronic state of most singly-charged molecular cations is typically bound,
21 either covalently or through the leading, attractive terms of the long-range electrostatic
22 interactions series. The corresponding Rydberg states are thus also bound, with spectral
23 positions following approximately Rydberg's formula

$$\tilde{\nu} = \frac{E_1(\alpha^+)}{hc} - \frac{RZ^2}{(n - \delta_\ell)^2}. \quad (1)$$

24 In Equation (1), $\tilde{\nu}$, $E_1(\alpha^+)$, R , Z , and δ_ℓ represent, respectively, the term value of the
25 Rydberg state, the ionization energy of the molecule leading to the formation of the cation
26 in state α^+ , the Rydberg constant, the charge number of the ion core (i.e., $Z = 1$ for neutral
27 molecules), and the quantum defect of the Rydberg states with orbital angular momentum
28 quantum number ℓ .

29 This overall picture of Rydberg states is also valid for molecular cations, however, with
30 two qualitative differences, discussed here with the example of a diatomic cation AB^+ , for
31 which the ionization energy of A is higher than the ionization energy of B, as illustrated in
32 Fig. 1. Firstly, removal of an electron from AB^+ leads to a dication ($Z = 2$ in Eq. (1)).
33 Depending on whether the ionization energy of A is higher than that of B^+ or not, the ground
34 state of the dication AB^{2+} is bound and correlates asymptotically to $A + B^{2+}$ (see Fig. 1(a))
35 or strongly repulsive and correlates asymptotically to $A^+ + B^+$ (see Fig. 1(b)). Between
36 these two limiting cases, several intermediate cases can be distinguished¹¹, characterized
37 by (avoided) curve crossings between the attractive ((i) in Fig. 1) and repulsive ((ii) in

38 Fig. 1) potential-energy curves, and by specific dynamical behaviors ranging from strongly
39 predissociative to thermodynamically stable (see Fig. 2 of Ref. 11). Secondly, Rydberg states
40 with a doubly-charged ion core AB^{2+} exhibit a broader range of dynamical phenomena than
41 those with a singly-charged ion core. Whereas Rydberg series with ion-core character (i)
42 in Fig. 1 follow Eq. (1) with $Z = 2$ and correlate diabatically to dissociation asymptotes
43 $A + [B^{2+}]nl$, those with ion-core character (ii) may follow Eq. (1) with either $Z = 1$ or
44 2 depending on the value of n and the internuclear distance and may correlate to either
45 $[A^+]nl + B^+$ or $A^+ + [B^+]nl$. Near-resonant charge-transfer processes are ubiquitous in
46 this case. The Rydberg series with ion-core characters (i) and (ii) may overlap spectrally
47 and interact, leading to situations where the decay processes can be simultaneously thought
48 of as predissociation, autoionization and charge transfer.

49 Molecular systems of the kind depicted in Fig. 1(a) are the most promising for experimen-
50 tal studies of Rydberg states of molecular cations. At the lowest n values, one indeed expects
51 most electronic states of the singly-charged cation to support metastable rovibrational levels
52 because of the bound nature of the electronic ground state of AB^{2+} and the attractive long-
53 range electrostatic interactions between the fragments. One can further anticipate that the
54 alignment of the Rydberg-electron orbital with respect to the internuclear axis affects the
55 bond strengths and the equilibrium internuclear separations of the corresponding molecular
56 states more strongly than is the case in neutral systems. Resonant multiphoton excitation
57 sequences through these metastable, low- n Rydberg states thus offers the prospect of access-
58 ing higher-lying Rydberg series of the cations over a broad range of internuclear separation
59 and energies, all the way to the second ionization thresholds.

60 $MgAr^+$ is an ideal system for a global investigation of the Rydberg states of a molecular
61 cation. The lowest molecular states of $MgAr^+$ derived from Mg^+ 3s, 3p, and 3d configura-
62 tions possess Rydberg character in the sense of Mulliken¹² and their overall energy structure
63 follows that of Mg^+ . The ionization energy of Ar ($127109.842(4) \text{ cm}^{-113}$) lies higher than
64 that of Mg^+ ($121267.65(6) \text{ cm}^{-114}$), corresponding to the situation depicted in Fig. 1(a).
65 $MgAr^+$ has only 29 electrons and accurate *ab initio* calculations can be carried out, also for
66 electronically excited states, to guide the experimental investigations. Potential energy func-
67 tions have been reported for several of the low-lying electronic states of $MgAr^+$ ¹⁵⁻²². These
68 states can be labeled by the state of the Mg^+ or Ar^+ ion at the dissociation asymptote in
69 addition to the usual letters and term symbols used to designate electronic states of diatomic

70 molecules. In this nomenclature, the first electronic states of MgAr^+ are the $\text{Mg}(3s)\text{Ar}^+$ X^+
71 $^2\Sigma^+$, $\text{Mg}(3p_\pi)\text{Ar}^+$ A^+ $^2\Pi_{1/2}$ and $^2\Pi_{3/2}$, and $\text{Mg}(3p_\sigma)\text{Ar}^+$ B^+ $^2\Sigma^+$ states, which are referred
72 to below as X^+ , $A_{1/2}^+$, $A_{3/2}^+$, and B^+ states. These labels are independent of the angular-
73 momentum coupling cases, which depend on the internuclear separation, as discussed in
74 Section IV A. The $A_{1/2}^+$, $A_{3/2}^+$, and B^+ states form the 3p Rydberg complex discussed in this
75 article. The Rydberg states of MgAr^+ associated with the Mg^+ 3p, 3d and 4s dissociation
76 asymptotes are easily accessible from the X^+ ground state through single-photon or reso-
77 nant two-photon excitation processes involving commercial UV lasers (see Fig. 2). The first
78 electronically excited state, the A_Ω^+ ($\Omega = 1/2, 3/2$) state, has a binding energy of more than
79 0.5 eV and an equilibrium internuclear distance of 2.40 Å. It is metastable, and several of its
80 vibrational levels have been observed by high-resolution spectroscopy²³⁻²⁷. The other mem-
81 ber of the 3p Rydberg complex, the B^+ state, is expected from calculations to be only very
82 weakly bound and to have a much larger equilibrium separation (ca. 4.37 Å, see Section III
83 below). In case of a sufficiently long lifetime of the B^+ state, the members of the 3p complex
84 would provide a set of intermediate states ideally suited to access higher Rydberg states of
85 MgAr^+ over a broad range of internuclear distances. The complete characterization of this
86 complex, which is the subject of this article and the companion article²⁸, represents the first
87 step in our efforts toward obtaining a global picture of the Rydberg series of a molecular
88 cation.

89 The present article reports on the experimental observation of the B^+ state of MgAr^+
90 and on the characterization of its structure and predissociation dynamics. The experimental
91 setup and methods used to record spectra of the B^+ state and to study its predissociation
92 are described in Section II. Section III presents the computational methods that have been
93 used to calculate the potential-energy functions of the low-lying electronic states of MgAr^+
94 *ab initio*. The experimental data obtained on the B^+-X^+ band system, which include
95 high-resolution spectra for the determination of rovibrational level energies and fragment
96 time-of-flight spectra for the determination of dissociation energies and β parameters, are
97 presented, analyzed and discussed in Section IV. These data, together with similar data
98 obtained on the A^+-X^+ band system of MgAr^+ , form the basis of the global analysis of the
99 3p Rydberg complex of MgAr^+ summarized in the companion article²⁸. Together, these two
100 articles complete our first step toward the characterization of the Rydberg spectrum of a
101 molecular cation.

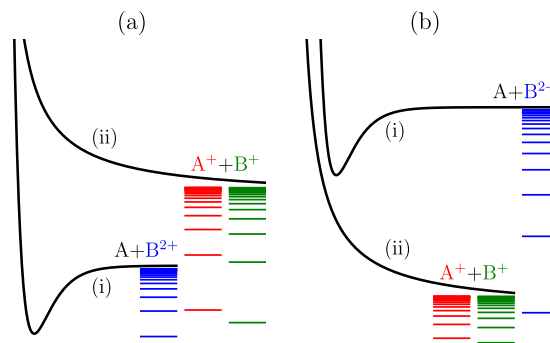


FIG. 1. Schematic representation of the electronic states of AB^{2+} dissociating in $A + B^{2+}$ and $A^+ + B^+$ fragments for the cases where the ionization energy of B^+ is lower than that of A (panel (a)) and vice-versa (panel (b)). The horizontal bars indicate atomic Rydberg series converging to the atomic ions A^+ (red), B^+ (green), and B^{2+} (blue).

102 II. EXPERIMENT

103 The experimental setup has been described in detail in Refs. 14,29. It consists of a
 104 laser-ablation source of Mg atoms, two Nd:YAG-pumped pulsed dye lasers (pulse duration
 105 ~ 5 ns), and a detection system for the photoions produced following photoexcitation. In
 106 the source, the ablated atoms were entrained in a supersonic beam of Ar, in which MgAr
 107 molecules were formed in the $Mg(3s3p)Ar\ a^3\Pi_0$ state and rotationally cooled to below 5
 108 K. The formation of MgAr in the metastable $Mg(3s3p)Ar\ a^3\Pi_0$ state was first described by
 109 Bennet *et al.*³⁰, who used a similar laser-ablation source and also observed the MgAr singlet
 110 ground state³¹. The molecular beam passed through a 3-mm-diameter skimmer and entered
 111 the photoexcitation chamber, where it was intersected by two laser beams at right angles.
 112 Photoexcitation took place within an electrode stack that allowed the application of pulsed
 113 electric fields to field ionize high Rydberg states and extract photoions into a time-of-flight
 114 (TOF) mass spectrometer at the end of which they were detected using a micro-channel
 115 plate (MCP).

116 The output of the first laser was frequency-tripled using two BBO crystals and set to
 117 a wave number $\tilde{\nu}_1 = 39334.8\text{ cm}^{-1}$. The frequency-tripled radiation had a bandwidth of
 118 $\sim 0.15\text{ cm}^{-1}$ and the laser pulse energy was ~ 0.5 mJ. The wave number $\tilde{\nu}_2$ of the second
 119 laser, after frequency doubling with a BBO crystal, was tunable in the range from 36100 to
 120 36700 cm^{-1} . The frequency-doubled radiation had a bandwidth of $\sim 0.1\text{ cm}^{-1}$, the beam

This is the author's peer reviewed, accepted manuscript. However, the online version of record will be different from this version once it has been copyedited and typeset.
PLEASE CITE THIS ARTICLE AS DOI:10.1063/1.50015603

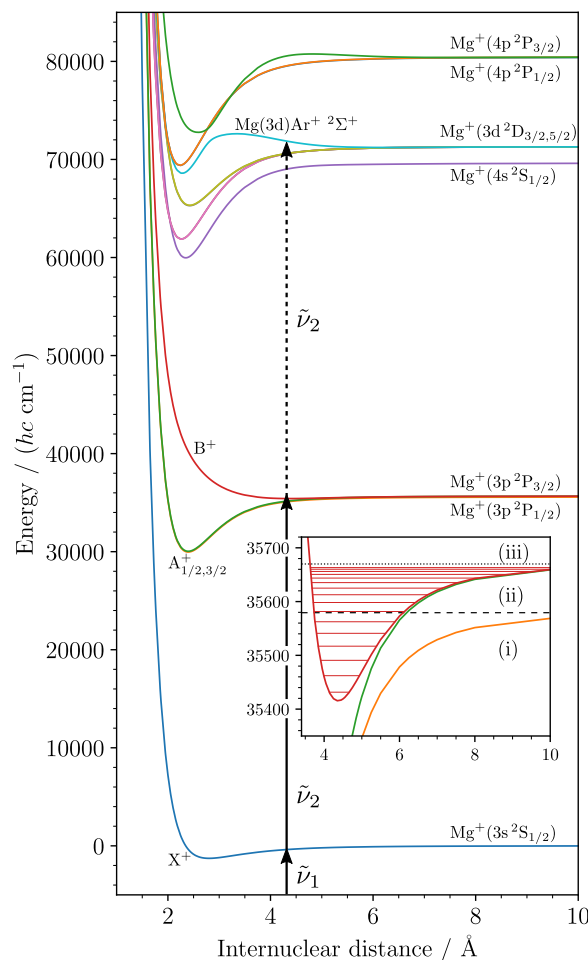


FIG. 2. Potential-energy curves of the ground and lowest-lying excited states of MgAr^+ obtained from relativistic EOM-CCSD/X2Cmmf/5Z* calculations. The inset presents an enlargement of the B^+ state curve. The configuration and term symbol of the resulting Mg^+ ion in the asymptotic limit are indicated for each group of molecular electronic states. Ar is in its 1S_0 ground state in each case. The solid arrows indicate the laser excitation scheme used in the experiment and the dashed arrow presents a possible pathway of resonant multiphoton dissociation. The spectral regions designated (i), (ii), and (iii) in the inset are introduced in Section IV B.

121 diameter was ~ 1 mm, and the pulse energy could be adjusted from below $1 \mu\text{J}$ up to ~ 0.5
122 mJ. The wave numbers of the lasers were calibrated using a commercial wavemeter with a
123 specified absolute accuracy of 0.02 cm^{-1} .

124 The first laser was used to excite MgAr to $[\text{X}^+(v'' = 7)]n\ell$ Rydberg states with principal
125 quantum numbers around $n \sim 135$. After ~ 10 ns, the ionic core of the MgAr Rydberg

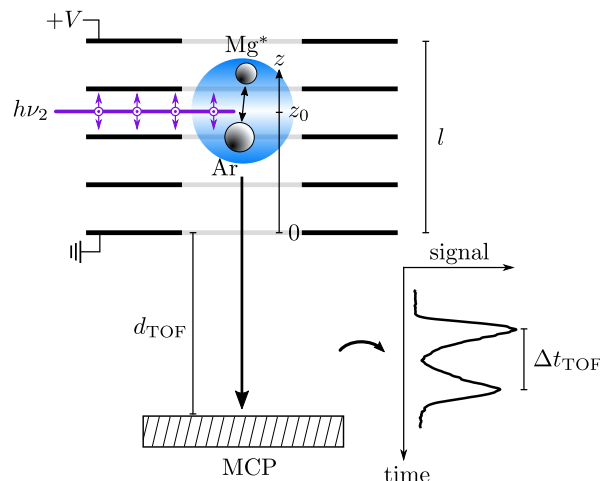


FIG. 3. Schematic representation of the photoexcitation region and the TOF mass spectrometer. After excitation with the second laser (indicated by ν_2) the MgAr molecules dissociate at position z_0 and the Mg-Rydberg-fragment cloud expands until the atoms are ionized by a pulsed electric field, which accelerates the Mg^+ ions to the MCP. The angular distribution of the dissociation products leads to TOF spectra such as the one shown at the bottom right (see text for details).

126 molecules was excited from the $X^+(v'' = 7)$ to the B^+ state using the second laser (see solid
 127 arrow in Fig. 2). Dissociation of the ion core in the B^+ state, either by direct or indirect
 128 mechanisms as discussed below, led to the formation of Mg atoms in high Rydberg states²⁷.
 129 Photoions generated in the photoexcitation region by the laser pulses (prompt ions) could
 130 be separated from the Mg Rydberg atoms by applying a $\sim 5\text{-}\mu\text{s}$ -long electric-field pulse of
 131 -1.7 V/cm , the magnitude of which is not large enough to efficiently field ionize Rydberg
 132 states with $n \sim 135$. A subsequent electric-field pulse with field strengths in the range
 133 from 50 to 170 V/cm field ionized the Rydberg states for detection. The spatial separation
 134 of the high Rydberg states and the prompt ions enabled us to distinguish them by their
 135 times of flight. Recording the pulsed-field-ionization yield of Mg^+ as a function of the laser
 136 wave number allowed the background-free measurement of transitions from a state-selected
 137 vibrational level of the X^+ electronic ground state of MgAr^+ to electronically excited levels,
 138 in the present case the $\text{MgAr}^+ B^+$ state²⁷.

139 Using extraction field pulses of 50 V/cm we observed a structure in the TOF spectrum of
 140 field-ionized Mg^+ ions reflecting the velocity and the angular distribution of the dissociation
 141 products. The situation is depicted schematically in Fig. 3, which presents the photoexcita-

tion region and the TOF mass spectrometer. Neutral Mg Rydberg fragments flying towards
or away from the detector had different times of flight because of (i) the different distances to
the detector after dissociation resulting from the $\sim 5 \mu\text{s}$ cloud expansion following photoex-
citation, and (ii) the different extraction potentials they were subjected to, resulting from
the different positions in the electrode stack. In the case where the dissociation fragments
were preferentially released along the extraction axis, two distinct peaks were observed in
the TOF spectrum, an example of which is shown at the bottom right of Fig. 3. Conversely,
in the case where the dissociation fragments were preferentially released perpendicular to
the extraction axis, only one broad peak was observed in the TOF spectrum.

We developed a model that allowed us to determine from the TOF spectra the angular
distribution of the dissociation fragments and the kinetic-energy release (KER) resulting
from the dissociation. The velocity of the Mg^+ fragments after the dissociation is related to
the KER by

$$v = \sqrt{\frac{2 \cdot \text{KER} \cdot m_{\text{Ar}}}{m_{\text{Mg}}(m_{\text{Mg}} + m_{\text{Ar}})}}, \quad (2)$$

where m_{Mg} and m_{Ar} are the masses of Mg and Ar, respectively. We designate the position
of the dissociation event in the electrode stack as z_0 (see Fig. 3) and the difference between
the time at which dissociation occurs and the time at which the large electric field pulse
is applied to field ionize the Rydberg atoms and accelerate the ions toward the detector as
 Δt_{prep} . The vertical position z of the Mg^+ fragments in the stack at the time of extraction
is given by

$$z = z_0 + \Delta t_{\text{prep}}(v \cos \theta_z - v_{\text{beam}}), \quad (3)$$

where θ_z is the angle between the z axis and the direction of dissociation, and v_{beam} is the
velocity of the molecular beam. The time of flight t_{TOF} resulting from an extraction field
with magnitude $F(= V/l)$ is in good approximation given by

$$t_{\text{TOF}}(z) = t_0 + \frac{d_{\text{TOF}} + 2z}{\sqrt{2qFz/m_{\text{Mg}}}}, \quad (4)$$

where t_0 is the extraction time, d_{TOF} is the distance between the electrode stack and the
MCP, and $q = +e$ is the charge of Mg^+ . The angular distribution of the fragments after
one-photon direct dissociation is given by³²

$$dI(\Omega) = \frac{I_0}{4\pi} [1 + \beta P_2(\cos \theta)] d\Omega, \quad (5)$$

where I_0 is the total intensity, β is the anisotropy parameter, θ denotes the angle between the direction of dissociation and the direction of polarization of the laser beam, P_2 is the Legendre polynomial of second order, and $d\Omega$ denotes the solid angle. In our experiments, the laser polarization was either parallel or perpendicular to the z axis. Using Eqs. (3) and (4), and integrating over the azimuthal angle around the z axis, we can express dI as a function of t_{TOF} , which, for a laser polarization parallel to the z axis, gives

$$dI(t_{\text{TOF}}) = \frac{I_0}{2\Delta t_{\text{prep}}v} \left[1 + \beta P_2 \left(\frac{z(t_{\text{TOF}}) - z'_0}{\Delta t_{\text{prep}}v} \right) \right] \left| \frac{dz}{dt_{\text{TOF}}} \right| dt_{\text{TOF}}. \quad (6)$$

167 In Eq. (6), $z'_0 = z_0 - \Delta t_{\text{prep}}v_{\text{beam}}$. The expression for $dI(t_{\text{TOF}})$ when the laser polarization
168 is perpendicular to the z axis is obtained by replacing β by $-\beta/2$ in Eq. (6) (see Appendix
169 A). The finite intersection volume of the molecular and the laser beams has a significant
170 effect on the TOF spectra and was taken into account following the procedure presented in
171 Appendix A, which consisted in summing the TOF profiles originating from different parts
172 of the photoexcitation volume. After a baseline correction with a second-order polynomial,
173 we could determine β and the KER in a nonlinear least-squares fit of the experimental TOF
174 spectra. The extraction time t_0 and the effective distance d_{TOF} (see Eq. (4)) of the electrode
175 stack to the MCP were calibrated by matching simulated TOF spectra to experimental TOF
176 spectra recorded at known KERs.

177 The model described above relies on the use of Eq. (5), which is not valid for multiphoton
178 dissociation³³. Therefore, we also used an alternative method for determining the KER,
179 which is independent of the exact form of the angular distribution. The KER is related to
180 the photon wave number $\tilde{\nu}_2$ and the dissociation limit E_{D} (given in the wave number unit
181 cm^{-1}) by $\text{KER}/(hc) = \tilde{\nu}_2 - E_{\text{D}}$. We consider the case where the laser polarization is parallel
182 to the z axis. By defining $\Delta t_{\text{TOF}} = t_{\text{TOF}}(z(\theta)) - t_{\text{TOF}}(z(-\theta))$, where $t_{\text{TOF}}(z)$ is defined as
183 in Eq. (4), we find for Δt_{TOF} a function of the form

$$\Delta t_{\text{TOF}}^2(\tilde{\nu}_2) = a^2(\tilde{\nu}_2 - E_{\text{D}}) + b^2(\tilde{\nu}_2 - E_{\text{D}})^3 + 2ab(\tilde{\nu}_2 - E_{\text{D}})^2, \quad (7)$$

184 in the limit of low KER. The TOF differences Δt_{TOF} can be determined from experimental
185 TOF spectra as shown in Fig. 3. The quantities a , b , and E_{D} were determined in a nonlinear
186 least-squares fit of Eq. (7) to Δt_{TOF} values measured at different wave numbers $\tilde{\nu}_2$.

187 III. QUANTUM CHEMICAL CALCULATIONS

188 A. Computational methodology

189 To characterize the ground and low-lying excited states of the MgAr^+ ion, we carried
190 out relativistic *ab initio* calculations with *variationally* treated spin-orbit coupling (SOC)
191 at various Mg-Ar internuclear distances. As wave-function models we chose relativistic
192 equation-of-motion coupled-cluster with singles and doubles excitations (EOM-CCSD)³⁴,
193 Kramers-restricted multi-reference configuration interaction with singles and doubles exci-
194 tations (KR-MRCI-SD)^{35,36}, and relativistic matrix product states (MPS) optimized with the
195 density-matrix-renormalization-group (DMRG) algorithm^{37,38}. All three models have differ-
196 ent advantages and disadvantages. Whereas the EOM-CCSD calculations are considered to
197 be very accurate in combination with a large single-particle basis set, the multi-reference and
198 DMRG calculations probe the validity of the EOM-CCSD wave-function model, but require
199 us to resort to smaller basis sets so that only semi-quantitative accuracy can be achieved in
200 the latter calculations.

201 All DMRG and KR-MRCI-SD calculations were carried out within a four-component
202 Dirac Hamiltonian framework including two-electron Coulomb contributions (denoted as
203 Dirac-Coulomb (DC) in the following) and with uncontracted aug-cc-pVDZ basis sets³⁹
204 (denoted as DZ*) for Mg and Ar, respectively. Furthermore, they share a common refer-
205 ence wave function which was obtained from an average-of-configuration self-consistent-field
206 calculation⁴⁰ for the open-shell MgAr^+ ion, namely by taking into account all possible con-
207 figurations of one electron in 26 Kramers-paired spinors. In the ensuing correlation step,
208 all electrons originating from the outer-valence Ar 3p as well as Mg 3s shell were correlated
209 in an orbital space spanned by 47 Kramers pairs (corresponding to 94 molecular spinors).
210 In contrast to the DMRG approach, the correlation space for the KR-MRCI-SD approach
211 was further divided into two orbital spaces. For KR-MRCI, the reference space comprised
212 all spinors of the Ar 3p shell as well as the corresponding 26 spinors of the average-of-
213 configuration space of the preceding self-consistent-field step. The second orbital space then
214 contained all remaining, energetically lowest-lying 62 spinors while taking into account at
215 most singles and doubles excitations between the two orbital spaces. The DMRG calcula-
216 tions delivered a full configuration interaction model in the given orbital space and served as

217 a qualitative reference for the KR-MRCI-SD model near the dissociation limit at an inter-
218 nuclear distance of $R = 50 \text{ \AA}$. In the relativistic DMRG calculations, the maximum virtual
219 bond dimension m was set to $m = 1024$ in combination with orbitals ordered according to
220 their energy, a maximum of 15 back-and-forward sweeps as well as a random guess for the
221 initial MPS.

222 For the EOM-CCSD model, a closed-shell reference wave function was obtained for each of
223 the three distinct cases described below from self-consistent-field calculations for a doubly-
224 ionized MgAr^{2+} molecular ion. This allowed us to calculate the electronic ground and
225 electronically excited states of MgAr^+ as electron attached states to MgAr^{2+} . We then
226 performed three types of EOM-CCSD calculations: the first one, EOM-CCSD/DC/2Z*,
227 comprised the same Hamiltonian, DZ*-type one-particle basis sets and a correlation space
228 of seven electrons in 94 spinors as described above for the KR-MRCI-SD and DMRG mod-
229 els. In contrast, our second set takes into account the full correlation space, i.e., correlat-
230 ing all 29 electrons of the MgAr^+ molecular ion in the complete set of molecular spinors
231 spanned by the atom-centered, uncontracted DZ*-type basis sets for Mg and Ar. Finally,
232 our third type of EOM-CCSD calculations, denoted as EOM-CCSD/X2Cmmf/5Z*, was
233 based on a molecular-mean-field (mmf) exact-two-component (X2C) Hamiltonian⁴¹ includ-
234 ing two-electron Coulomb and Gaunt contributions in combination with very large, fully
235 uncontracted aug-cc-pV5Z basis sets³⁹ (denoted as 5Z*) for Mg and Ar (similar to the sec-
236 ond set, all electrons of Mg (ion) and Ar (atom) were correlated within the set of molecular
237 spinors up to an energy threshold of 100 Hartree that result from the 5Z* basis sets for Mg
238 and Ar in their uncontracted form).

239 All EOM-CCSD as well as the KR-MRCI-SD calculations were carried out with a de-
240 velopment version of the DIRAC19 program package^{42,43}. This program also provides an
241 interface that steers relativistic DMRG calculations with the DMRG software package QC-
242 MAQUIS^{38,44,45}. Molecular constants have been derived by a least-squares fit of the potential
243 energy curves to a fifth-order polynomial by means of the TWOFIT utility program available
244 in DIRAC19.

245 B. Numerical results

246 Table I presents the atomic low-lying excited-state spectrum of Mg^+ at the dissociation
247 limit of MgAr^+ , as obtained from molecular KR-MRCI-SD/DC/DZ*, DMRG/DC/DZ*, and
248 EOM-CCSD/DC/DZ* and EOM-CCSD/X2Cmmf/5Z* calculations carried out at an inter-
249 nuclear distance of $R = 50 \text{ \AA}$. The calculated excited-state data for Mg^+ is in general in
250 reasonably good agreement with the corresponding reference data taken from the standard
251 NIST atomic spectra database⁴⁶. As expected, we find a clear improvement of the calculated
252 results when switching from the small DZ* basis sets to the basis set limit achieved by the
253 uncontracted 5Z* basis set.

254 As can be seen from Table I, the largest absolute deviation of $\sim 1700 \text{ cm}^{-1}$ (corresponding
255 to a relative error of 2.5 %) with respect to the reference data is found for the 4s excited
256 state of Mg^+ in case of the EOM-CCSD/DC/DZ* model, and similarly, for the KR-MRCI-
257 SD/DC/DZ* and DMRG/DC/DZ* approaches. The DMRG data exactly matches with KR-
258 MRCI-SD for the Mg excited states because these states are effectively one-electron states at
259 the dissociation limit with little to no Ar 3p correlation contributions. In other words, both
260 approaches yield results of near full-configuration-interaction quality for the Mg-dominated
261 states at the dissociation limit because of the chosen correlation space. The situation changes
262 for the charge-transfer states which will be discussed in future work.

263 The deviation of 2.5% reduces to less than 0.3% for our EOM-CCSD/X2Cmmf/5Z* ref-
264 erence model. Further comparison with the EOM-CCSD/DC/DZ* model illustrates that
265 this considerable improvement within our reference model is a combined result of both
266 the enlarged one-particle basis sets and the inclusion of core-valence and core-core electron
267 correlation. For example, solely taking into account the latter correlation effects within
268 the EOM-CCSD/DC/DZ* approach (seventh column in Table I) reduces the relative error
269 to only 1.9% for the previously discussed 4s excited state of Mg^+ . Moreover, resorting
270 to fully uncontracted aug-cc-pCV5Z basis sets^{47,48} (c5Z*, not shown in Table I), which
271 include in addition to the 5Z* sets of primitive functions optimized tight core-polarizing
272 basis functions, further reduces the deviation for the 4s excited state of Mg^+ from 0.3%
273 (EOM-CCSD/X2Cmmf/5Z*) to 0.1% (EOM-CCSD/X2Cmmf/c5Z*). In general, we find
274 that the inclusion of tight core-polarizing basis functions improves the description of the
275 Mg-dominated excited states, i.e., leading to an even closer agreement with the reference

276 data, with excitation-energy shifts ranging from 35 cm⁻¹ (3s⁰3p¹ ²P term) to 158 cm⁻¹
277 (3s⁰3d¹ ²D term).

278 Particularly noteworthy is that all computational approaches considered in this work
279 yield spin-orbit splittings of both low-lying ²P atomic terms, corresponding to a 3s⁰3p¹ and
280 3s⁰4p¹ configuration of the Mg⁺ ion, respectively, that are in excellent agreement with their
281 respective experimental reference values as shown in Table I.

TABLE I. Energy levels of the Mg⁺ ion obtained from molecular four-component KR-MRCI-SD/DC/DZ*, DMRG/DC/DZ* and EOM-CCSD/DC/DZ* as well as molecular-mean-field two-component EOM-CCSD/X2Cmmf/5Z* calculations for MgAr⁺ at an internuclear distance of $R = 50$ Å. All term values are reported relative to the ground state in cm⁻¹.

Conf.	Term	J	Method ^a					Reference ^b
			KR-MRCI-SD/ DZ*	DMRG/ DZ*	EOM-CCSD/ DZ*	EOM-CCSD/ DZ* ^c	EOM-CCSD/ 5Z*	
3s	² S	1/2	0.0	0.0	0.0	0.0	0.0	0.0
3p	² P	1/2	34703	34703	34680	35013	35579	35669
		3/2	34793	34793	34769	35104	35670	35761
4s	² S	1/2	68131	68131	68097	68494	69618	69805
3d	² D	5/2	70861	70861	70818	71300	71294	71490
		3/2	70861	70861	70819	71300	71295	71491
4p	² P	1/2	80308	80308	80270	80735	80411	80620
		3/2	80344	80344	80306	80772	80442	80650

^a The notation indicating the dependence on the Hamiltonian has been dropped in the labelling of the methods.

^b Data taken from the NIST Basic Atomic Spectra Database, see Ref. 46.

^c EOM-CCSD/DC/DZ* calculations with full correlation space.

282 Figure 2 shows the low-lying potential energy curves of the ground and lowest-lying
283 excited states of MgAr⁺ obtained with EOM-CCSD/X2Cmmf/5Z* approach. Note that
284 we here only consider those electronic states of the MgAr⁺ ion which correspond in the
285 asymptotic limit to an argon atom in its ground state and a Mg⁺ ion in its ground and excited
286 state up to a Mg⁺ 3s⁰4p¹ configuration. Electronic states with predominant Ar → Mg⁺

287 charge-transfer character, which correspond in the asymptotic limit to an Ar^+ ion ($3s^2p^5\ ^2P$
288 term) and a $\text{Mg}(3s^2)$ ground-state atom, will be discussed in future work.

289 As can be understood in view of Fig. 2, the lowest-lying electronically excited $^2\Pi$ and $^2\Sigma^+$
290 states arise from excitations to a Mg^+ $3p$ orbital which can exhibit perpendicular (p_π) and
291 parallel (p_σ) orientations with respect to the molecular axis. Hence, electrostatic interactions
292 in the excited $A_{1/2,3/2}^+$ states are expected to be relatively strong because of the orientation
293 of the involved $\text{Mg } p_\pi$ orbital, which effectively exposes a doubly positive Mg core to the
294 Ar atom⁴⁹. In contrast, as a result of on-axis electron-density contribution originating from
295 the occupation of on-axis σ -type orbitals, electrostatic binding is reduced in the $\text{Mg } 3s$ -
296 like X^+ ground and excited $3p_\sigma$ -like B^+ states. In the latter, a greater shielding is to be
297 expected relative to the ground state⁴⁹. Consequently, we expect the $A_{1/2,3/2}^+$ states to be
298 more strongly bound than the X^+ ground state, giving rise to a redshift of the $A_{1/2,3/2}^+ \leftarrow$
299 X^+ electronic transitions with respect to the atomic resonance line. Likewise, as a result
300 of weaker electrostatic interactions, the excited B^+ state is more weakly bound than the
301 ground state. The latter implies a blue-shifted $B^+ \leftarrow X^+$ transition relative to the atomic
302 resonance⁴⁹. Similar qualitative considerations hold for the higher-lying $^2\Sigma$, $^2\Pi_{1/2,3/2}$, and
303 $^2\Delta_{3/2,5/2}$ states of MgAr^+ that correlate in the asymptotic limit with an Ar ground-state
304 atom and a $\text{Mg}^+(4s)$, $\text{Mg}^+(3d)$, and $\text{Mg}^+(4p)$ excited-state ion, respectively.

305 In agreement with the above qualitative considerations, inspection of Fig. 2 reveals that
306 the spin-orbit split $\Omega = 1/2$ and $\Omega = 3/2$ components of the $A_{1/2,3/2}^+$ state are more strongly
307 bound than the X^+ ground state. In addition, we find that their excited-state equilibrium
308 internuclear distance of $R_e(A^+) = 2.396 \text{ \AA}$ is considerably shorter than the predicted ground-
309 state equilibrium internuclear distance of $R_e(X^+) = 2.803 \text{ \AA}$. Both of these results are
310 therefore consistent with the qualitatively expected redshift of the $A_{1/2,3/2}^+ \leftarrow X^+$ electronic
311 transitions discussed above. Based on these findings, our EOM-CCSD/X2Cmmf/5Z* data
312 yield an estimate for the $A^+ \leftarrow X^+$ transition of 31402 cm^{-1} . This value agrees very well with
313 the corresponding data for the spin-orbit averaged $\tilde{\nu}_{00}$ transition of 31477 cm^{-1} obtained from
314 resonance-enhanced multiphoton dissociation measurements²⁷. Considering the calculated
315 $\tilde{\nu}_{00}$ transition as a reference, we therefore predict a redshift in the MgAr^+ spectrum for the
316 corresponding $\text{Mg}^+ 3p\ ^2P_{1/2,3/2} \leftarrow 3s\ ^2S_{1/2}$ transition in the bare ion to be approximately
317 4300 cm^{-1} . Our calculated result matches closely the experimental data mentioned above,
318 which yield a redshift of 4253 cm^{-1} . Moreover, our estimate for the dissociation energy

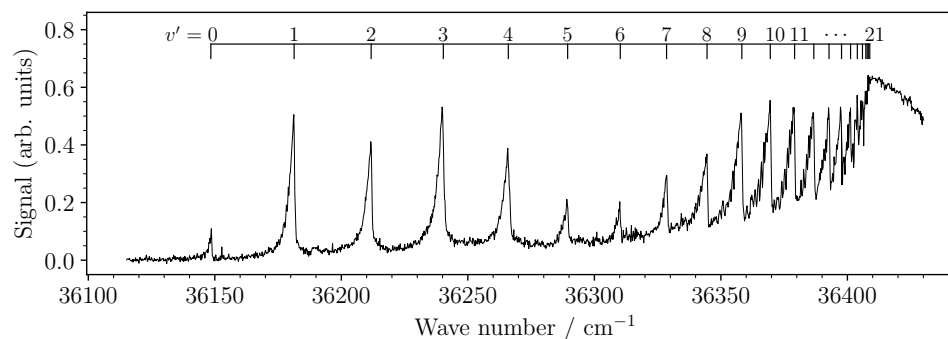


FIG. 4. Overview spectrum of the $^{24}\text{MgAr}^+ \text{B}^+(v') \leftarrow \text{X}^+(v'' = 7)$ transition recorded at high laser-pulse energies (~ 0.5 mJ per pulse). The sharp rise around 36409 cm^{-1} indicates the onset of the dissociation continuum of the B^+ state. In this spectrum, only vibrational levels up to $v' = 17$ are resolved. The positions of the remaining vibrational levels, indicated along the assignment bar, were derived from the high-resolution spectrum shown in Fig. 6.

319 $D_0 = 1220.2 \text{ cm}^{-1}$ of the X^+ ground state is in very good agreement with the experimental
320 estimate of $D_0 = 1246.0(12) \text{ cm}^{-1}$ reported in the companion article²⁸.

321 Turning to the excited-state manifold corresponding in the asymptotic limit to a Mg^+
322 $3s^03d^1$ configuration as shown in Fig. 2, we find that the spin-orbit splitting of the $^2\Pi$ and
323 $^2\Delta$ states is too small to resolve the spin-orbit-split components in the figure. In agreement
324 with the qualitative considerations given above, the $^2\Pi_{1/2,3/2}$ and $^2\Delta_{3/2,5/2}$ states (displayed
325 with yellow and pink lines in Fig. 2, respectively) are more strongly bound than the X^+
326 state because of the off-axis electron density that results from the occupation of $3d_\pi$ - or
327 $3d_\delta$ -like orbitals of the Mg^+ ion. Interestingly, the $^2\Sigma$ state originating from a $\text{Mg}^+ 3s^03d^1$
328 configuration (cyan line) undergoes an avoided crossing at an internuclear distance of ~ 2.8
329 Å, with a higher-lying $^2\Sigma$ state (upper green line) that correlates in the asymptotic limit to
330 a $\text{Mg}^+ 3s^04p^1$ configuration.

331 IV. EXPERIMENTAL RESULTS AND DISCUSSION

332 A. Energy level structure

333 We have measured the photodissociation spectrum of the $\text{MgAr}^+ \text{X}^+(v'' = 7)$ state
334 via the $\text{B}^+(v')$ state using the method of isolated-core (multi)photon Rydberg-dissociation

335 spectroscopy²⁷. Our measurements include overview spectra of the complete vibrational pro-
336 gression of the B⁺ state as well as high-resolution measurements of each vibrational band,
337 in which the rotational structure could be partially resolved. The assignment of the vibra-
338 tional quantum number was derived from the comparison with the corresponding spectrum
339 of ²⁶MgAr⁺ (not shown), as explained below.

340 Figure 4 depicts an overview spectrum of the ²⁴MgAr⁺ B⁺(*v*') ← X⁺(*v*'' = 7) transitions
341 recorded at high laser-pulse energies (~ 0.5 mJ per pulse). The vibrational progression
342 exhibits a drop in intensity around *v*' = 6 and extends all the way to the dissociation
343 continuum, the onset of which is indicated by a rise in signal around 36409 cm⁻¹. The
344 intensity maxima of the strongest vibrational bands, in particular *v*' = 1, 3, and *v*' ≥ 9, are
345 approximately the same, which suggests that the spectrum was recorded under saturating
346 conditions, which were necessary to observe all vibrational levels of the B⁺ state, especially
347 those of low *v*' value. Although the overview spectrum in Fig. 4 only allows the unambiguous
348 assignment of B⁺ levels up to *v*' = 17, several levels beyond *v*' = 17 could be identified with
349 the help of spectra recorded at lower pulse energies and higher resolution (see below). The
350 analysis of the vibrational intensity distribution is presented in Section IV D.

351 To assign the vibrational quantum numbers, we determined the positions $\tilde{\nu}^i(v')$ (*i* =
352 24, 26) of the band maxima for both ²⁴MgAr⁺ and ²⁶MgAr⁺ and extracted the isotopic
353 shifts of the B⁺(*v*') levels using

$$\Delta\tilde{\nu}(v') = \Delta_a + (\tilde{\nu}_{X^+}^{24}(7) - \tilde{\nu}_{X^+}^{26}(7)) + (\tilde{\nu}^{24}(v') - \tilde{\nu}^{26}(v')). \quad (8)$$

354 In Eq. (8), $\Delta_a = 0.38$ cm⁻¹ is the isotopic shift of the MgAr a ³Π₀(*v* = 0) state, estimated
355 from the results of *ab initio* calculations reported in Ref. 21, and $\tilde{\nu}_{X^+}^i(v'' = 7)$ denote the
356 ^{*i*}MgAr⁺ X⁺(*v*'' = 7) ← ^{*i*}MgAr a ³Π₀(*v* = 0) transition wave numbers^{29,50}. For instance, the
357 isotopic shift we observed for *v*' = 7 is $\Delta\tilde{\nu}(7) = 3.3(3)$ cm⁻¹. This standard analysis of
358 isotopic shifts⁵¹ did not only yield an unambiguous vibrational assignment but also values
359 for the harmonic ($\omega_e = 35.43(30)$ cm⁻¹) and anharmonic ($\omega_e x_e = 1.21(20)$ cm⁻¹) vibrational
360 constants of the ²⁴MgAr⁺ B⁺ state, which adequately describe the observed structure up to
361 *v*' = 12.

362 The upper panel of Fig. 5 shows a spectrum of the B⁺(1) ← X⁺(7) band recorded at
363 high resolution. The spectrum exhibits a strong line on the high-wave-number side and a
364 progression of transitions to different rotational states of the B⁺ state levels with intensities

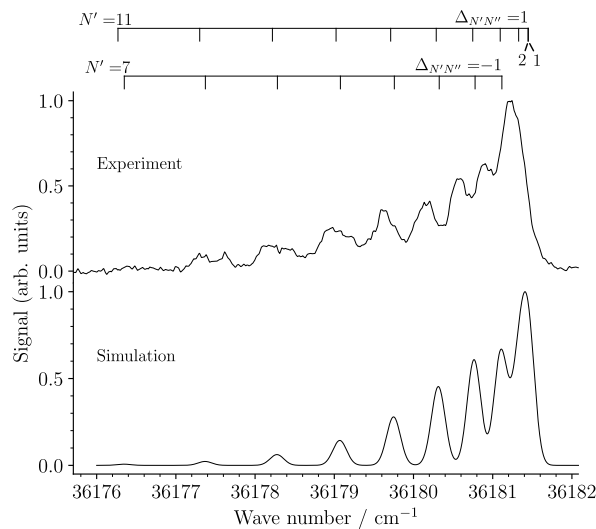


FIG. 5. High-resolution spectrum of the $\text{MgAr}^+ \text{B}^+(v' = 1) \leftarrow \text{X}^+(v'' = 7)$ band. The initial and the final states are well described by Hund's case (b), leading to two branches that overlap in the spectrum. The branches are denoted by $\Delta_{N'N''} = N' - N'' = 1$ (R-Branch) and $\Delta_{N'N''} = -1$ (P-Branch), where N'' and N' are the rotational-angular-momentum quantum numbers of the initial and final states, respectively. The simulation was performed assuming a rotational temperature of 2 K.

365 decreasing towards the low-wave-number end of the spectrum. This spectrum is typical of
 366 what we observed for transitions to the lowest vibrational levels of the B^+ state. Beyond
 367 $v' = 7$ the spectra revealed a different rotational structure, examples of which are shown in
 368 the upper panel of Fig. 6 for $v' \geq 13$. In this region, the vibrational bands comprise more
 369 lines. We attribute this change to the increasing importance of the spin-orbit interaction
 370 as the internuclear separation R increases and the resulting mixing of the B^+ and $\text{A}_{1/2}^+$
 371 states at large R values. This mixing leads to a transition from Hund's case (b) at short
 372 internuclear distances and low values of v' , characterized by integer values of the rotational-
 373 angular-momentum quantum number N' , to Hund's case (c) at large internuclear distances
 374 and high values of v' , characterized by half-integer values of the total angular momentum
 375 quantum number J' . A complete model of the spin-orbit interaction in the $\text{Mg}(3p)\text{Ar}^+$
 376 Rydberg complex is presented in the companion article²⁸.

377 For each of the $v' = 0 - 3$ and $v' = 7 - 16$ bands we were able to identify several isolated
 378 rotational lines and determined their positions $\tilde{\nu}$ by fitting them with Gaussian line-shape

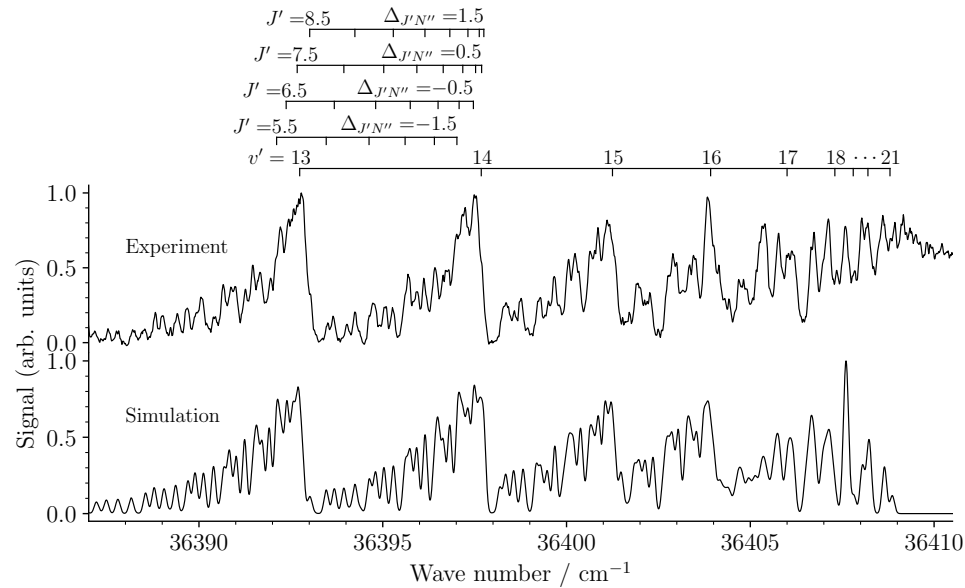


FIG. 6. High-resolution spectrum of the $\text{MgAr}^+ \text{B}^+(v' = 13 - 21) \leftarrow \text{X}^+(v'' = 7)$ bands. In this range, the final states are well described by Hund's case (c), leading to four rotational branches. The branches are denoted by half-integer values of $\Delta_{J'N''} = J' - N''$, where N'' is the rotational-angular-momentum quantum number of the initial state and J' is the total angular momentum of the final states. The simulation was performed assuming a rotational temperature of 3 K.

379 functions. We then determined rotational constants and the band origin $\tilde{\nu}_{v',7}$ by performing
380 nonlinear least-squares fits of the appropriate expression for the transition energy. Because of
381 the progressive evolution of the rotational structure from Hund's case (b) at low v' values to
382 Hund's case (c) at high v' values, the choice of the appropriate Hund's case for intermediate
383 v' , namely $v' = 8 - 12$, was not completely unambiguous. Up to $v' = 8$, we used the following
384 expression,

$$\tilde{\nu} = \tilde{\nu}_{v',7} + B'_{v'} N'(N' + 1) - B''_7 N''(N'' + 1), \quad (9)$$

385 describing a Hund's-case-(b)-to-Hund's-case-(b) transition at the low N' and N'' values
386 probed experimentally. In Eq. (9), $B'_{v'}$, N' and B''_7 ($= 0.1121 \text{ cm}^{-128}$), N'' are the rota-
387 tional constants and rotational quantum numbers of the final and initial states, respectively.
388 The band origins and rotational constants determined in this way are listed in Table II and
389 were used to calculate the spectra for comparison with experimental results. An example is
390 shown for $v' = 1$ in Fig. 5 for a rotational temperature of 2 K. The spectrum consists of
391 two overlapping branches, denoted by $\Delta_{N',N''} = N' - N''$ above the assignment bars. The

392 $\Delta_{N'N''} = 0$ branch is missing as expected for a $\Sigma^+ - \Sigma^+$ transition. The degradation of
 393 the band intensity profile toward low wave numbers results from the different rotational
 394 constants of the initial ($B_7'' = 0.1121 \text{ cm}^{-1}$) and final states ($B_1' = 0.0550 \text{ cm}^{-1}$). Whereas
 395 the calculated spectrum in Fig. 5 assumes a thermal distribution, the experimental spec-
 396 trum was recorded from the nonthermal distribution generated with the laser driving the
 397 $X^+(7) \leftarrow a^3\Pi_0$ transition. Therefore the intensity distribution of the calculated spectrum
 398 does not reliably describe the measured intensity distribution, and the effect is particularly
 399 pronounced near the R-branch bandhead.

400 Beyond $v' = 8$, we used the standard expression for transitions between a Hund's case
 401 (b) initial level and a Hund's case (c) final level,

$$\tilde{\nu} = \tilde{\nu}_{v'7} + B_{v'}' [J'(J' + 1) - \Omega'^2] - B_7'' N''(N'' + 1), \quad (10)$$

402 where J' is the total angular momentum of the final state and $\Omega' = 1/2$. The band origins
 403 and rotational constants determined in least-squares fits based on Eq. (10) are given in Table
 404 II. Calculations of the rotational structure of Hund's-case-(b)-to-Hund's-case-(c) transitions
 405 for $v' \geq 13$ at a rotational temperature of 3 K are shown in the lower panel of Fig. 6, with
 406 explicit rotational assignments for the $v' = 14$ band. Each band consists of four branches,
 407 denoted $\Delta_{J'N''} = J' - N''$, instead of two at low v' , which explains the different appearance
 408 of the bands observed at low and high v' values.

409 For the $v' = 4 - 6$ vibrational states we could not resolve individual rotational lines. To
 410 determine the band origins listed in Table II, we simulated the band contours assuming a
 411 Hund's-case-(b)-to-Hund's-case-(b) transition and rotational constants obtained by polyno-
 412 mial interpolation of the rotational constants listed in Table II, and shifted the calculated
 413 spectra along the wave-number axis until agreement with the experimental observations was
 414 reached. From the $B_{v'}'$ values determined for the $v' = 0 - 8$ vibrational levels, a B_e value of
 415 $0.0608(7) \text{ cm}^{-1}$ was derived. This corresponds to an equilibrium bond length R_e of $4.301(25)$
 416 \AA , which is in reasonable agreement with the theoretical value of 4.374\AA , presented in Sec-
 417 tion III. From the origin of the $B^+(0) \leftarrow X^+(7)$ band ($\tilde{\nu}_{07} = 36148.43(20)$) and the onset of
 418 the dissociation continuum in Fig. 6, i.e., $E_D = 36409.0(10) \text{ cm}^{-1}$, we estimate the dissocia-
 419 tion energy of the B^+ state to be $D_0 = 260.6(10) \text{ cm}^{-1}$. Using the vibrational constants listed
 420 above, we derive an equilibrium dissociation energy of $D_e = D_0 + \omega_e/2 - \omega_e x_e/4 = 278.0(10)$
 421 cm^{-1} for the B^+ state. These values of D_0 and D_e are in reasonable agreement with the

422 values of 237.7 cm^{-1} and 253.2 cm^{-1} , respectively, predicted theoretically and reported in
423 Section III. Given the weakly-bound nature of the B^+ state, further diffuse basis functions
424 might be required in the respective atomic basis sets for Mg and Ar to further improve the
425 accuracy of our reference EOM-CCSD/X2Cmmf/5Z* model described in detail in Section
426 III.

427 The vibrational bands with $v' \geq 17$ lie so close to each other that their rotational struc-
428 tures overlap. It is therefore not possible to assign rotational lines to specific vibrational
429 bands in this range nor to use Eq. (10) to determine band origins and rotational con-
430 stants. Instead, we estimated the rotational constants using a polynomial extrapolation of
431 the values given in Table II and successively added the contributions of Hund's-case-(b)-to-
432 Hund's-case-(c) transitions with increasing v' value to reproduce the experimental spectrum.
433 In this process, the band origins were adjusted to give the best agreement between experi-
434 ment and simulation, as given in Table II. Although the simulation allows the identification
435 of a few individual rotational lines, we could not determine rotational constants of the final
436 states with $v' \geq 17$ in this way, because they are so small that the rotational structure of
437 the spectra is essentially determined by the rotational constant of the initial state.

438 The data presented in Table II and in Figs. 4–6 provide a complete picture of all bound
439 levels of the $\text{MgAr}^+ B^+$ state and forms the basis for the global analysis of the $\text{Mg}(3p)\text{Ar}^+$
440 Rydberg complex discussed in Ref. 28.

441 B. Dissociation mechanisms

442 We have measured the TOF spectra associated with the KER and angular distributions
443 of the dissociation products for the $B^+ v' = 0 - 5$, $v' = 8 - 13$ states, and above the B^+
444 dissociation limit up to 36700 cm^{-1} . All measurements were performed for parallel and
445 perpendicular laser polarizations with respect to the TOF axis.

446 A selection of TOF spectra is presented in the upper panel of Fig. 7. In all TOF spectra
447 that were recorded with the laser polarization parallel to the TOF axis, we observed two
448 distinct peaks, which are well suited for the determination of the KER, whereas in the case
449 of perpendicular polarization, the TOF distributions consisted of a single broad peak. In
450 the remainder of this section, we focus the discussion on the spectra measured with the
451 laser polarization parallel to the TOF axis, although similar considerations also apply to the

TABLE II. Measured values $\tilde{\nu}_{v'7}$ of the observed $B^+(v') \leftarrow X^+(v'' = 7)$ transitions and the respective vibrational term values $T_{v'}$ and rotational constants $B_{v'}$ of the final states. All values are in cm^{-1} .

v'	$\tilde{\nu}_{v'7}$	$T_{v'}$	$B_{v'}$	v'	$\tilde{\nu}_{v'7}$	$T_{v'}$	$B_{v'}$
0	36148.43(20)	0.00(28)	0.0608(10)	11	36379.13(20)	230.70(28)	0.0324(10)
1	36181.34(20)	32.91(28)	0.0550(20)	12	36386.73(20)	238.30(28)	0.0293(10)
2	36211.78(20)	63.35(28)	0.0543(10)	13	36392.74(20)	244.31(28)	0.0212(10)
3	36240.31(20)	91.88(28)	0.0521(10)	14	36397.68(20)	249.25(28)	0.0203(10)
4	36265.99(20)	117.56(28)	0.050 ^a	15	36401.25(20)	252.82(28)	0.0187(10)
5	36289.44(20)	141.01(28)	0.048 ^a	16	36403.92(20)	255.49(28)	0.0190(20)
6	36310.23(20)	161.80(28)	0.045 ^a	17	36405.95(40)	257.52(45)	0.013 ^b
7	36328.53(20)	180.10(28)	0.0420(10)	18	36407.28(40)	258.85(45)	0.010 ^b
8	36344.53(20)	196.10(28)	0.0388(10)	19	36407.80(40)	259.37(45)	0.007 ^b
9	36358.28(20)	209.85(28)	0.0359(10)	20	36408.25(40)	259.82(45)	0.005 ^b
10	36369.52(20)	221.09(28)	0.0358(10)	21	36408.85(40)	260.42(45)	0.005 ^b

^a Estimated by interpolation of the other measured rotational constants $B_{v'}$.

^b Estimated by extrapolation of the other measured rotational constants $B_{v'}$.

452 spectra recorded with the polarization perpendicular to that axis. Starting from $v' = 0$ and
 453 up to $v' = 5$ one observes an increase in the separation Δt_{TOF} of the two peaks. At $v' = 8$
 454 the TOF profiles abruptly change to a much narrower distribution, which broadens again for
 455 increasing vibrational levels. As the B^+ dissociation limit is crossed, one observes another
 456 sudden narrowing of the TOF distribution followed by a broadening as the wave number of
 457 the laser increases. These observations suggest that different dissociation mechanisms are
 458 at play in the three spectral regions (i) $v' = 0 - 5$, (ii) $v' = 8 - 13$, and (iii) above the
 459 dissociation limit. For each measured TOF spectrum, we determined the associated KER
 460 using the models described in Section II. In the regions (i) and (ii), the KERs were averaged
 461 over three independent measurements. The KERs are shown as a function of the laser wave
 462 number in the lower panel of Fig. 7, in which the three regions described above are labeled
 463 with (i), (ii), and (iii). These regions are also depicted in the inset of Fig. 2.

464 In region (iii), direct photodissociation into the B^+ continuum takes place. The dissoci-

This is the author's peer reviewed, accepted manuscript. However, the online version of record will be different from this version once it has been copyedited and typeset.
PLEASE CITE THIS ARTICLE AS DOI:10.1063/1.5015603

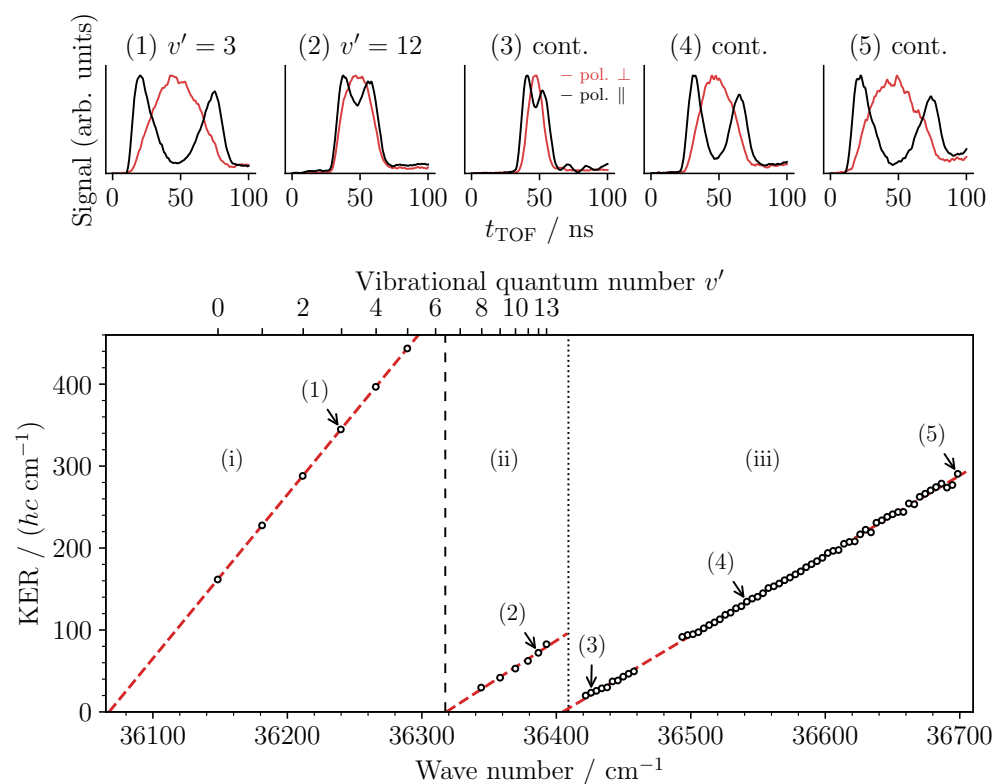


FIG. 7. Upper panels: Typical TOF spectra recorded with laser polarization parallel (black) and perpendicular (red) to the TOF axis. The lower panel shows the KER determined from the TOF spectra as a function of the laser wave number, which suggests different dissociation mechanisms for the regions (i)–(iii). The vertical dashed line indicates the dissociation limit of the $A_{1/2}^+$ state and the vertical dotted line indicates the dissociation limit of the B^+ state of MgAr^+ . The labels (1)–(5) indicate the positions at which the TOF spectra presented in the upper panels were recorded.

465 ation threshold $E_{\text{D}}(B^+ \leftarrow X^+(7)) = 36408.6(10) \text{ cm}^{-1}$ of the B^+ state with respect to the
 466 $X^+(v'' = 7)$ state, shown as dotted vertical line in Fig. 7, is accurately known from the
 467 analysis of the spectra presented in the companion article²⁸. Therefore, the KER and thus
 468 the Mg^+ fragment velocity v are known accurately and the measurements in region (iii) were
 469 used to calibrate the values of the model parameters t_0 and d_{TOF} in Eq. (4), which were
 470 not known accurately. The data points displayed in region (iii) correspond to the analysis
 471 using Eq. (6). Their linear extrapolation to zero KER (red dashed line) yields a dissociation
 472 threshold of $E_{\text{D}} = 36404.7(7) \text{ cm}^{-1}$, where the specified error does not include systematic

473 errors but corresponds to the 1σ uncertainty of the extrapolation. The gap of data points
474 around 36480 cm^{-1} originates from the fact that the photodissociation cross section is too
475 small in this range to record TOF spectra with sufficient signal-to-noise ratio.

476 In region (ii), the TOF measurements were analyzed using Eq. (6) and the values of t_0 and
477 d_{TOF} determined in region (iii). The extrapolation of the KER to zero yielded a dissociation
478 threshold with respect to the $X^+(v'' = 7)$ state of $E_D = 36318(2)\text{ cm}^{-1}$, where the specified
479 error corresponds to an uncertainty of 1σ of the fit. This value is in good agreement with the
480 $\text{Mg}^+(3p\ ^2P_{1/2}) + \text{Ar}(^1S_0)$ dissociation asymptote of the $A_{1/2}^+$ state, which lies at $36317.0(10)$
481 cm^{-1} ²⁸ and is shown as a vertical dashed line in Fig. 7. In region (ii), the $A_{1/2}^+$ dissociation
482 continuum is accessible by predissociation from the $B^+(v')$ states through the nonadiabatic
483 effects caused by the spin-orbit interaction. Hence, the predissociation has the same origin
484 as the transition from Hund's case (b) to Hund's case (c) of the B^+ state discussed in Section
485 IV A, namely the mixing of the B^+ and $A_{1/2}^+$ states induced by the spin-orbit interaction.

486 In region (i), the TOF measurements were analyzed using Eq. (7). We first fitted
487 the parameters a and b of Eq. (7) to Δt_{TOF}^2 values measured in region (iii) and subse-
488 quently kept these parameters fixed to determine the dissociation threshold E_D from the
489 KERs measured in region (i). The fit was only successful when assuming a two-photon
490 dissociation, i.e., replacing $\tilde{\nu}_2$ by $2\tilde{\nu}_2$ in Eq. (7). The two-photon dissociation thresh-
491 old with respect to the $X^+(v'' = 7)$ state was determined to be $E_D = 72135(5)\text{ cm}^{-1}$
492 (the specified uncertainty corresponds to 1σ of the fit). This value is in good agree-
493 ment with the expected positions of the $\text{Mg}^+(3d\ ^2D_{3/2,5/2}) + \text{Ar}(^1S_0)$ dissociation asymp-
494 totes at $72138.8(10)\text{ cm}^{-1}$ and $72137.9(10)\text{ cm}^{-1}$, respectively, calculated using the cycle
495 $E_D(B^+ \leftarrow X^+(7)) + E(\text{Mg}^+ 3d\ ^2D_{3/2,5/2}) - E(\text{Mg}^+ 3p\ ^2P_{3/2})$ and atomic term values from
496 Ref. 46. The two-photon excitation, indicated by a dashed arrow in Fig. 2, takes place
497 to the repulsive part of the $\text{Mg}(3d)\text{Ar}^+\ ^2\Sigma^+$ state, and causes dissociation to the $\text{Mg}^+(3d\ ^2D_{3/2,5/2}) + \text{Ar}(^1S_0)$
498 asymptotes. In principle, two-photon dissociation is also possible in
499 region (ii). However, in the TOF spectra we recorded, two-photon dissociation only gave
500 rise to a broad and weak background, which suggests that two-photon dissociation is much
501 less efficient than predissociation at the laser intensities used to record the TOF spectra.

502 Our data thus unambiguously reveal three distinct dissociation mechanisms over a range
503 of only $\sim 300\text{ cm}^{-1}$. In region (i), the molecules dissociate following two-photon resonance-
504 enhanced absorption, producing Mg^+ ions in the $3d\ ^2D_{3/2,5/2}$ states. In region (ii), they

This is the author's peer reviewed, accepted manuscript. However, the online version of record will be different from this version once it has been copyedited and typeset.
PLEASE CITE THIS ARTICLE AS DOI:10.1063/1.50015603

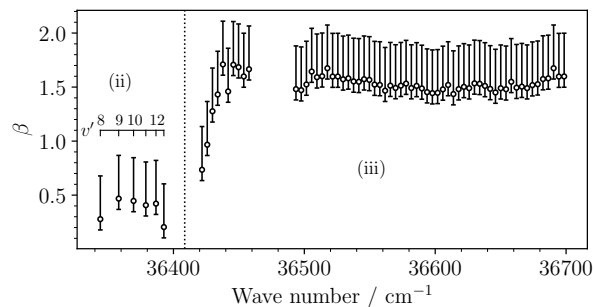


FIG. 8. Experimentally determined values of the anisotropy parameter β for regions (ii) and (iii) of the spectrum of the $B^+(v') \leftarrow X^+$ transition of $MgAr^+$. The markedly different values of β in the two regions originate from the different dissociation mechanisms that occur in these regions.

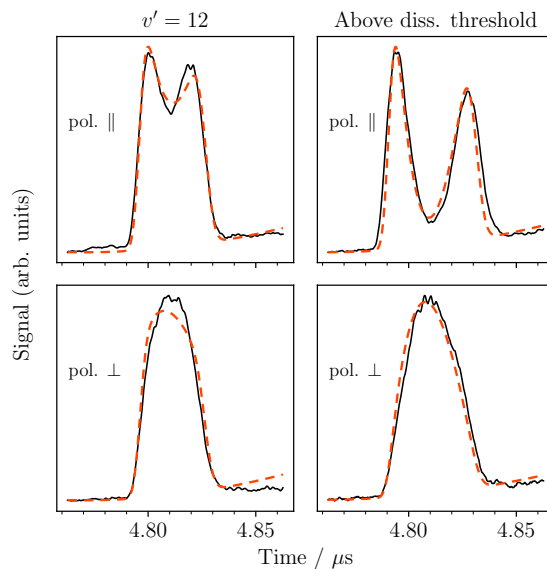


FIG. 9. Examples of TOF spectra observed following dissociation of $MgAr^+$ and the corresponding fits based on Eq. (6) (dashed line) to determine the KER and β for $v' = 12$ and in the continuum at 36542.8 cm^{-1} . The fit parameters for the cases where the laser was polarized perpendicular to the TOF axis (lower panels) are the same as for the cases where the laser was polarized parallel to the TOF axis (upper panels), except for an overall intensity factor. The fits in the left and right columns correspond to $\beta \approx 0.4$ and ~ 1.6 , respectively.

505 predominantly predissociate into the $A_{1/2}^+$ continuum, producing Mg^+ ions in the $3p \ ^2P_{1/2}$
506 state. In region (iii), fragmentation occurs by direct photodissociation into the B^+ contin-
507 uum, producing Mg^+ ions in the $3p \ ^2P_{3/2}$ state.

508 **C. Dissociation dynamics and angular distributions**

509 In the analysis of the TOF spectra presented in Fig. 7 for regions (ii) and (iii), we also
 510 obtained the values of the anisotropy parameter β , which are presented in Fig. 8. Figure
 511 9 shows, as examples, the results of fits based on Eq. (6) to TOF spectra measured at
 512 the position of the predissociating $v' = 12$ level (36386.6 cm^{-1} , left column) and above the
 513 dissociation threshold at 36542.8 cm^{-1} (right column), respectively. The fits (dashed line)
 514 were performed using the spectra recorded with the laser polarized parallel to the TOF axis
 515 (upper panels). For $v' = 12$ we obtained a β value of 0.4, which is typical for the values
 516 we determined for predissociating states. In region (ii), the values of β were averaged over
 517 three independent measurements for each value of v' , and varied between ~ 0.2 and ~ 0.5 ,
 518 with an average of 0.4, as shown on the left-hand side of Fig. 8.

519 In the continuum (region (iii)), we typically determined β values between ~ 1.4 and ~ 1.7
 520 with an average of $\beta \approx 1.5$, as illustrated on the right-hand side of Fig. 8. The fit shown
 521 in the upper right panel of Fig. 9 corresponds to β value of 1.6. The origin of the rather
 522 different β parameters in regions (ii) and (iii) is discussed below. The spectra in the lower
 523 panels of Fig. 9 were recorded with the laser polarization perpendicular to the TOF axis
 524 under otherwise identical conditions, and the only parameter that was adjusted in the fit
 525 was the overall intensity I_0 . The same β values thus adequately describe the measurements
 526 carried out with parallel and perpendicular polarization.

527 In direct dissociation, one approaches the axial-recoil limit, $\beta = 2$, for sufficiently low
 528 angular momenta and sufficiently high KERs³². In the case of a $^1\Sigma - ^1\Sigma$ transition, this limit
 529 corresponds to a difference $\delta_{N''+1} - \delta_{N''-1} = \pi$ of the phase shifts of the continuum nuclear
 530 wavefunctions accessed from a given initial-state rotational level with rotational quantum
 531 number N'' in the expression derived by Zare³²,

$$\beta \approx \frac{2(N''^2 + N'' + 1) - 6N''(N'' + 1) \cos(\delta_{N''+1} - \delta_{N''-1})}{(2N'' + 1)^2}. \quad (11)$$

532 In the present case we consider the transition between a $^2\Sigma$ state and a mixed $^2\Sigma_{1/2} - ^2\Pi_{1/2}$
 533 state, which has predominantly $^2\Sigma_{1/2}$ character in the relevant range of internuclear distances
 534 (see below). We therefore do not expect a strong deviation from $^1\Sigma - ^1\Sigma$ photodissociation
 535 because of the weakly coupled nature of the electron spin. From the internuclear potential
 536 determined in the companion article²⁸, we computed the phase shifts of the continuum
 537 wavefunctions using Numerov's method⁵² and obtained the values of β by averaging them

538 over the initial-state rotational distribution at 3 K. For a KER of 12 cm^{-1} , which corresponds
539 to the lowest KER considered in the analysis of region (iii), we obtained $\beta = 1.88$. For higher
540 KER we calculated $\beta \gtrsim 1.9$, with monotonically increasing values of β for increasing KERs.
541 At a KER of 300 cm^{-1} , corresponding to the highest KER considered in the analysis of region
542 (iii), we obtained $\beta = 1.98$. The β values determined experimentally are systematically lower
543 than the theoretical ones by about ~ 0.4 . We attribute this discrepancy to the fact that
544 our model for the TOF distributions does not perfectly reproduce the observed asymmetry
545 between the two lobes of the distributions nor the position of the minimum between these
546 lobes (see upper panels of 9). We thus believe that the fitted β values represent lower bounds
547 of the actual values. The experimental values of β determined in the continuum (~ 1.5) are
548 significantly higher than the value of 1.03 ± 0.05 determined at a KER corresponding to
549 cm^{-1} by Hoshino *et al.*⁵³.

550 The spin-orbit predissociation observed in the range from $v' = 7$ to the dissociation
551 threshold (region (ii)) leads to a markedly different angular distribution of the fragments
552 compared to direct dissociation, as reflected in the value of the measured anisotropy pa-
553 rameter $\beta \approx 0.4$. The fact that the rotational structure of the predissociative $B^+(v')$ states
554 is partially resolved (see Fig. 6) indicates that predissociation broadening is smaller than
555 the spacing of adjacent rotational energy levels. Classically this means that the timescale
556 associated with the rotational motion of the molecular ion is comparable to, or shorter than,
557 the predissociation lifetime. The anisotropy of the angular distribution is expected to be
558 reduced by the rotational motion compared to direct photodissociation in the axial-recoil
559 approximation⁵⁴. Moreover, the measured spectral lines do not exhibit asymmetric Fano
560 profiles, indicating that direct photoexcitation to the dissociation continuum ($A_{1/2}^+$ in the
561 present case) is negligible compared to excitation to levels of the B^+ state followed by predi-
562 sociation. A more detailed analysis of the lifetime of the predissociating states is presented
563 in the companion article²⁸.

564 Following a theoretical procedure similar to that introduced by Pernot *et al.*⁵⁵, the β
565 parameter associated with the excitation from a given $X^+(v'', N'')$ rovibrational level to a
566 $B^+(v', J')$ predissociative level can be expressed within second-order perturbation theory as
567 (see Appendix B)

$$\beta_{N''J'} = \frac{\sum_{J''} \beta_{J''J'} S(i\Lambda'' S'' N'' J''; e\Omega' J')}{\sum_{J''} S(i\Lambda'' S'' N'' J''; e\Omega' J')}. \quad (12)$$

568 In Eq. (12), $S(i\Lambda'' S'' N'' J''; e\Omega' J')$ is the transition line strength from a state described

569 by Hund's coupling case (b), with a projection quantum number of the orbital angular
570 momentum on the internuclear axis Λ'' , a spin angular momentum quantum number S'' ,
571 a total angular momentum quantum number without spin N'' , a total angular momentum
572 quantum number J'' , and a set of other good quantum numbers i , to a predissociative state
573 described by Hund's coupling case (c) with a total angular momentum quantum number
574 J' and its projection quantum number Ω' onto the internuclear axis, and a set of other
575 good quantum numbers e . The anisotropy parameters $\beta_{J''J'}$ associated with each $J' \leftarrow J''$
576 transitions are known analytically (see, e.g., Ref. 55), and tend to values of $\frac{1}{2}$ for $J' = J'' \pm 1$
577 (P and R branches) and -1 for $J' = J''$ (Q branch) in the limit of large J'' values. The total
578 $\beta_{N''J'}$ parameter is therefore the weighted sum of the β parameters of the transitions from
579 the various J'' sublevels of a given N'' level, with weights given by the relative strengths of
580 the different branches.

581 The transition line strengths $S(i\Lambda''S''N''J''; e\Omega'J')$ depend *a priori* on the extent of the
582 ${}^2\Sigma_{1/2} - {}^2\Pi_{1/2}$ mixing in the upper state, caused by spin-orbit interaction and responsi-
583 ble for the Hund's-coupling-case-(c) nature of the high vibrational levels of the B^+ state.
584 These case-(c) states, written as $|e\Omega'J'M'\rangle$, can be expanded in terms of case-(a) functions
585 $|e\Lambda'S'\Sigma'\Omega'J'M'\rangle$ as

$$|ev'\Omega'J'M'\rangle = \sum_{\Lambda'} c_{\Lambda'}(R) |e\Lambda'S'\Sigma'\Omega'J'M'\rangle, \quad (13)$$

586 where Σ' is the projection quantum number of the spin on the internuclear axis and M'
587 is the projection quantum number of the total angular momentum onto the z axis of the
588 laboratory-fixed frame. The R -dependent expansion coefficients $c_{\Lambda'}(R)$ are obtained by
589 diagonalization of the spin-orbit interaction matrix in the case (a) basis, as described in the
590 companion article²⁸. The transition line strengths $S(i\Lambda''S''N''J''; e\Omega'J')$ thus involve several
591 vibronic transition moments of the form

$$\int dR c_{\Lambda'}(R) \chi_{\Lambda'v'J'}^*(R) M_{\Lambda'}(R) \chi_{v''N''}(R), \quad (14)$$

592 where $\chi_{v''N''}$ and $\chi_{\Lambda'v'J'}$ are the vibrational wave functions of the initial and predissociative
593 states, respectively, and $M_{\Lambda'}(R)$ is the R -dependent electronic transition dipole moment.
594 The vibrational wave function of the initial $X^+(v'' = 7)$ state considered in the present
595 study has a nonnegligible amplitude only in the range from $R \approx 4.5 a_0$ to $R \approx 7.5 a_0$. In
596 this region, the $\Sigma - \Pi$ mixing is very small in the B^+ state and, to a good approximation,
597 $c_{\Lambda=0} = 1$ and $c_{|\Lambda|=1} = 0$. Therefore, the line strengths correspond to transitions from

598 Hund's-coupling-case-(b) ${}^2\Sigma^+$ states to Hund's-coupling-case-(a) ${}^2\Sigma_{1/2}^+$ states, which can be
599 calculated analytically⁵⁶. In this way, the anisotropy parameter $\beta_{N''J'}$ can be calculated for
600 arbitrary N'' and J' values.

601 The experimental β parameter for the $v' = 12$ vibrational band was recorded at a wave
602 number of 36386.60 cm^{-1} . Three rotational transitions lie within the 0.1 cm^{-1} laser band-
603 width, and the experimental result corresponds to the sum of the three individual $\beta_{N''J'}$
604 values (0.71, 0, and 0.70, respectively, in order of increasing wave number) weighted by the
605 product of the corresponding line intensities with the spectral intensity of the laser light
606 at the transition wave numbers (0.14, 0.16, and 0.70, respectively). The total calculated
607 β parameter is 0.58, in reasonable agreement with the experimental value of ~ 0.4 . A β
608 parameter of 0.5 is expected for high J' values (see above). However, for the low J' values
609 considered in the present case this argument is not valid and the origin of the $\beta = 0.5$ value
610 lies rather in the dynamic averaging caused by the overlapping rotational transitions. A sim-
611 ilar agreement between the measured and calculated anisotropy parameters was obtained
612 for the $v' = 8 - 13$ predissociating states.

613 D. Intensities of the vibronic transitions

614 Panels (a) and (b) in Fig. 10 present overview spectra of the $B^+ \leftarrow X^+(v'' = 7)$ transition
615 extending from $v' = 0$ up to $\sim 300\text{ cm}^{-1}$ above the dissociation threshold, recorded with
616 laser pulse energies of $\sim 0.5\text{ mJ}$ and $< 1\ \mu\text{J}$, respectively. We refer to them below as the
617 high-intensity and low-intensity spectra, respectively. In the regions designated (i)–(iii) in
618 Fig. 10, which are the same as in Fig. 7, these spectra exhibit very different patterns.

619 The high-intensity spectrum in regions (i) and (ii) in Fig. 10(a) is the same as in Fig. 4
620 and exhibits an intensity minimum around $v' = 6$. The continuum region (region (iii)) in
621 Fig. 10(a), i.e., above 36409 cm^{-1} , reveals an intensity minimum around 36480 cm^{-1} and a
622 broad maximum around 36600 cm^{-1} . The low-intensity spectrum, presented in Fig. 10(b),
623 only possesses nonzero intensity in region (ii).

624 The intensity patterns apparent in panels (a) and (b) of Fig. 10 can be explained with
625 the dissociation mechanisms described in Section IV B when considering the Franck-Condon
626 factors of the corresponding transitions. We have determined these factors using the po-
627 tential of the X^+ state published in Ref. 29, the potential of the B^+ state reported in the

This is the author's peer reviewed, accepted manuscript. However, the online version of record will be different from this version once it has been copyedited and typeset.
PLEASE CITE THIS ARTICLE AS DOI:10.1063/1.50015603

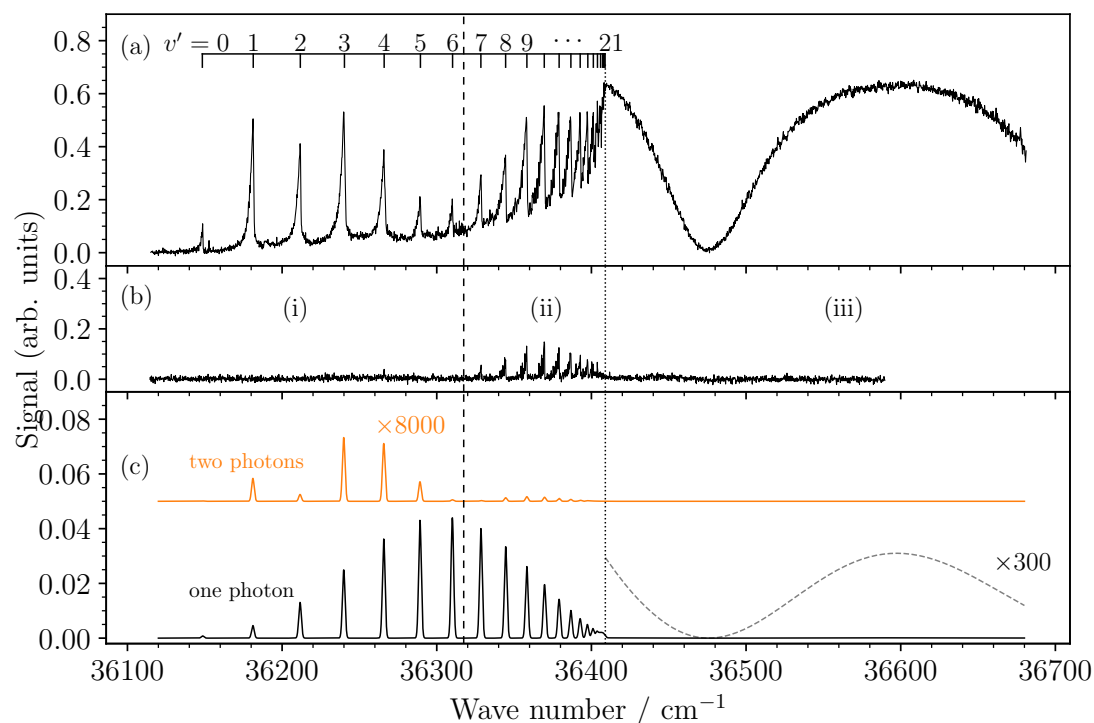


FIG. 10. Panels (a) and (b): Overview spectra of the $B^+(v') \leftarrow X^+(v'' = 7)$ transition of MgAr^+ recorded at laser pulse energies of $\sim 0.5 \text{ mJ}$ and $< 1 \mu\text{J}$, respectively. Panel (c): Two-photon (upper trace) and one-photon (lower trace) Franck-Condon factors, after convolution with a Gaussian lineshape function with a FWHM of 2 cm^{-1} . The Franck-Condon factors of the two-photon transitions and of the single-photon transition to the B^+ continuum (dashed curve) were scaled by 8000 and 300, respectively, to be visible on the scale of the figure (see text for details).

628 companion article²⁸, and the potential of the $\text{Mg}(3d)\text{Ar}^+ \ ^2\Sigma^+$ state calculated *ab initio*, as
 629 described in Section III (see also Fig. 2). The vibrational wavefunctions were calculated by
 630 solving the nuclear Schrödinger equation using a Legendre-Gauss-Lobatto discrete-variable-
 631 representation technique in combination with exterior complex scaling^{28,29,57–59}. The Franck-
 632 Condon factors of the $B^+ \leftarrow X^+$ one-photon transition and the $\text{Mg}(3d)\text{Ar}^+ \ ^2\Sigma^+ \leftarrow B^+ \leftarrow$
 633 X^+ resonant two-photon transition are shown in Fig. 10(c) as black and orange curves,
 634 respectively, after convolution with a Gaussian lineshape function with a FWHM of 2 cm^{-1} .
 635 In the latter case, the Franck-Condon factors represent products of the Franck-Condon fac-
 636 tor of the $B^+ \leftarrow X^+$ transition and of the Franck-Condon factor of the $\text{Mg}(3d)\text{Ar}^+ \ ^2\Sigma^+$
 637 $\leftarrow B^+$ bound-to-continuum transition determined as explained in Appendix C. To account

638 for the very different efficiencies of the different excitation processes, the Franck-Condon
639 factors of the two-photon transitions and of the direct dissociation (region (iii)) had to be
640 enhanced by factors of 8000 and 300, respectively, compared to the one-photon transitions
641 to the predissociative levels of the B^+ state. This analysis confirms that the high-intensity
642 spectrum in panel (a) was recorded under saturating conditions.

643 In region (i), the Franck-Condon factors calculated for the resonant two-photon tran-
644 sitions suggest that two-photon dissociation is much more efficient in this region than in
645 regions (ii) and (iii), as discussed in Section IV B. Moreover, they qualitatively reproduce
646 the drop in intensity towards $v' = 6$ observed in the high-intensity spectrum (Fig. 10(a))
647 and the weaker intensity of the transition to $v' = 2$.

648 In region (ii), the relative intensities of the observed lines are not well described by the
649 calculated Franck-Condon factors of the $B^+ \leftarrow X^+$ transition (black curve). In the case of
650 the high-intensity spectrum (Fig. 10(a)), we attribute the constant intensities of transitions
651 to the highest vibrational levels to the saturation of the transitions, whereas the relative
652 intensities measured in the low-intensity spectrum are governed by the predissociation dy-
653 namics. Except for $v' = 7$, the calculated predissociation widths also support this finding
654 (see supplementary material in the companion article²⁸). The fact that we observe a signal
655 in region (ii) but not in region (i) at low intensities is another indication of the proposed
656 one- and two-photon dissociation mechanisms, respectively.

657 The high-intensity spectrum (Fig. 10(a)) exhibits stronger maximal intensities in region
658 (iii) than in region (ii). Moreover, the lobe around 36600 cm^{-1} is significantly broader than
659 predicted by the Franck-Condon analysis. This behavior can also be explained by saturation.
660 Whereas in region (ii) the populations of the initial and final states equilibrate, in region (iii)
661 the entire initial-state population yield may be drained into the photodissociation continuum,
662 which leads to a higher Mg^+ yield. As described in the companion article²⁸, the spectrum in
663 region (iii) was used to optimize the repulsive part of the B^+ potential curve such that the
664 calculated positions of the intensity minimum and maximum matched the positions observed
665 experimentally. In the low-intensity spectrum (Fig. 10(b)) no dissociation products were
666 observed in region (iii), as expected from the low Franck-Condon factors.

667 V. CONCLUSIONS AND OUTLOOK

668 In this article, we have reported on the first step of a systematic investigation of the
669 Rydberg states of a molecular cation, MgAr^+ , which consisted in the observation and full
670 characterization of the $\text{B}^+ \ ^2\Sigma^+$ state of MgAr^+ located below the $\text{Mg}^+(3p \ ^2P_{3/2}) + \text{Ar}(^1S_0)$
671 dissociation threshold. This state and the two spin-orbit components ($\Omega = 1/2$ and $3/2$) of
672 the $\text{A}^+ \ ^2\Pi_\Omega$ state of MgAr^+ form a low-lying $3p$ Rydberg complex, which can be regarded
673 as the first stepping stone towards ionization¹² of MgAr^+ and the formation of the doubly-
674 charged ion MgAr^{2+} . Whereas previous theoretical work had emphasized the repulsive
675 nature of the B^+ state at short range²¹, new *ab initio* calculations carried out in the realm
676 of the present investigation indicated a potential well at long range ($R_e \approx 4.4 \text{ \AA}$) able to
677 support several vibrational levels.

678 Using the method of isolated-core (multi)photon Rydberg-dissociation spectroscopy²⁷, we
679 have recorded rotationally resolved spectra of transitions from the selected $\text{X}^+(v'' = 7)$ state
680 of MgAr^+ to all vibrational levels of the B^+ state from $v' = 0$ to 21, from which we have
681 extracted an extensive set of molecular constants. The rotational structure of the vibrational
682 levels of the B^+ state undergoes a transition from Hund's angular-momentum coupling case
683 (b) at low v' values to case (c) at high v' values, which we attribute to a mixing of the B^+
684 and $\text{A}_{1/2}^+$ states at large internuclear distances induced by the spin-orbit interaction.

685 We have also identified the mechanisms through which high Rydberg states of Mg are
686 produced following photodissociation of the isolated state-selected MgAr^+ ion core by mea-
687 suring the kinetic-energy release upon dissociation and the corresponding β parameters.
688 These mechanisms include (i) resonant two-photon dissociation, via the lowest vibrational
689 levels of the B^+ state, to the $\text{Mg}^+(3d \ ^2D_{3/2,5/2}) + \text{Ar}(^1S_0)$ dissociation continua accessed
690 through the repulsive branch of the potential of the $^2\Sigma^+$ state of the $3d$ complex; (ii) predis-
691 sociation of the vibrational levels of the B^+ state with $v' \geq 7$ to the $\text{Mg}^+(3p \ ^2P_{1/2}) + \text{Ar}(^1S_0)$
692 dissociation continuum mediated by the spin-orbit interaction; and (iii) direct photodissoci-
693 ation to the $\text{Mg}^+(3p \ ^2P_{3/2}) + \text{Ar}(^1S_0)$ continuum of the B^+ state. Finally, we have observed
694 a broad intensity oscillation in the photodissociation continuum of the B^+ , which we have
695 quantitatively interpreted in terms of Franck-Condon densities for bound-continuum transi-
696 tions (see Appendix C).

697 In the next steps of this investigation, we intend to present a global model of the $3p$

698 Rydberg complex of MgAr^{+28} and the analysis of isolated-core Rydberg-dissociation spectra
699 in the region of the 3d and 4s complexes.

700 ACKNOWLEDGMENTS

701 We thank J. A. Agner and H. Schmutz for technical support. This work is supported
702 financially by the Swiss National Science Foundation (Grant No. 200020-172620) and the
703 European Research Council through an advanced grant under the European Union's Horizon
704 2020 research and innovation programme (Grant No. 743121).

705 DATA AVAILABILITY STATEMENT

706 The data that support the findings of this study are available from the corresponding
707 author upon reasonable request.

708 Appendix A: Details of the analysis of the TOF distributions

709 In this section we provide the details of the derivation and application of Eq. (6). In order
710 to apply Eq. (5) to analyze TOF distributions recorded with a linear TOF spectrometer,
711 one needs to perform two subsequent changes of variables, namely $\theta \rightarrow z$ and $z \rightarrow t_{\text{TOF}}$.
712 The first transformation involves the integration over the azimuthal angle around the z axis
713 and depends on the laser polarization. We discuss the cases $\theta_z = \theta$ (polarization parallel to
714 the z axis) and $\theta_z = \theta + \pi/2$ (polarization perpendicular to the z axis) separately.

$\theta_z = \theta$: In the case of parallel polarization, we have $z - z'_0 = r \cos \theta$ and the surface element is $dzd\phi_z/r$, where $r = \Delta t_{\text{prep}}v$ and ϕ_z is the azimuthal angle of the angular distribution, which coincides with the azimuthal angle around the z axis. The angular distribution as a function of z can then be obtained by

$$\begin{aligned} dI(z) &= \int_0^{2\pi} \frac{I_0}{4\pi r} [1 + \beta P_2((z - z'_0)/r)] dzd\phi_z \\ &= \frac{I_0}{2r} [1 + \beta P_2((z - z'_0)/r)] dz. \end{aligned} \quad (\text{A1})$$

$\theta_z = \theta + \pi/2$: In the case of perpendicular polarization, we have $\cos \theta = \sqrt{r^2 - (z - z_0)^2}/r$.

$\sin \phi_z$ and the surface element is again $dzd\phi_z/r$. Integration over ϕ_z yields

$$\begin{aligned} dI(z) &= \\ &= \frac{I_0}{4\pi r} \int_0^{2\pi} \left[1 + \beta P_2 \left(\frac{\sqrt{r^2 - (z - z'_0)^2}}{r} \sin \phi_z \right) \right] dzd\phi_z \\ &= \frac{I_0}{2r} \left[1 - \frac{\beta}{2} P_2((z - z'_0)/r) \right] dz, \end{aligned} \quad (\text{A2})$$

715 which is identical to Eq. (A1) after replacing β by $-\beta/2$.

Inversion of Eq. (4) yields the required dependence of z on t_{TOF} for the second change of variables,

$$z(t_{\text{TOF}}) = \frac{(bt_{\text{TOF}}^2 - 4d_{\text{TOF}}) \pm \sqrt{(bt_{\text{TOF}}^2 - 4d_{\text{TOF}})^2 - 16d_{\text{TOF}}^2}}{8}, \quad (\text{A3})$$

716 where $b = 2qF/m_{\text{Mg}}$. The choice of sign in Eq. (A3) depends on how far the cloud of
717 dissociation products extends within the electrode stack. If the dissociation products exceed
718 $z = d_{\text{TOF}}/2$ one has to make a careful distinction between particles for which $z < d_{\text{TOF}}/2$
719 and particles for which $z > d_{\text{TOF}}/2$. In the present experiments, the condition $z < d_{\text{TOF}}/2$
720 was always fulfilled and thus only the negative sign in Eq. (A3) was relevant. Using

$$dz = \left| \frac{dz}{dt_{\text{TOF}}} \right| dt_{\text{TOF}}, \quad (\text{A4})$$

721 one obtains Eq. (6) from Eqs. (A1), (A3), and (A4).

722 Because the molecules occupy a finite volume rather than a single point z'_0 , one has to take
723 into account the initial distribution of photoexcited molecules by computing the weighted
724 sum

$$dI(t_{\text{TOF}}) = \int dI(t_{\text{TOF}}, z'_0) p(z'_0) dz'_0 \quad (\text{A5})$$

725 for each value of t_{TOF} . In Eq. (A5), $p(z'_0)$ is the distribution of dissociating molecules,
726 which is governed by the laser profile and is well described by a Gaussian distribution in our
727 experiment.

728 Appendix B: Predissociation angular distribution

729 The angular distribution of fragments following predissociation of a diatomic molecule
730 has been investigated by a number of authors^{33,54,55,60-62}. We follow here an approach similar

731 to those of Mukamel and Jortner⁶⁰ and Pernot *et al.*⁵⁵, which we adapted to the present
732 case. We consider the transition from an initial state described by Hund's coupling case
733 (b) to a final state described by Hund's coupling case (c) via a predissociative state also
734 described by Hund's coupling case (c). The initial state is denoted by $|i\Lambda''S''N''J''M''\rangle$ and
735 has an energy $E_{iN''}$. The final state is denoted by $|d\Omega\mathbf{k}\rangle$, where \mathbf{k} is the momentum vector
736 of the fragments corresponding to a KER of $\mu k^2/2$. The predissociative state is denoted by
737 $|e\Omega'J'M'\rangle$ and has the energy $E_{eJ'}$ and a predissociation rate $\Gamma_{eJ'}$. All wave functions are
738 expressed within the Born-Oppenheimer approximation. Within lowest-order perturbation
739 theory and neglecting direct excitation to the dissociation continuum, the differential cross
740 section $\frac{d\sigma}{d\Omega}$ for photodissociation by a photon with energy $\hbar\omega$ can be written as⁶⁰

$$\frac{d\sigma}{d\Omega} = \frac{(2\pi)^2}{\hbar c} \left| \sum_{eJ'M'} \frac{\langle d\Omega\mathbf{k}|H_v|e\Omega'J'M'\rangle \langle e\Omega'J'M'|\hat{\epsilon} \cdot \boldsymbol{\mu}|i\Lambda''S''N''J''M''\rangle}{E_{iN''} + \hbar\omega - E_{eJ'} + \frac{i}{2}\Gamma_{eJ'}} \right|^2. \quad (\text{B1})$$

741 The operator H_v represents the coupling from the intermediate state to the dissociation
742 continuum, and will be left unspecified in the following for the sake of generality. In the
743 present case, it represents the non-adiabatic spin-orbit coupling between the B^+ and $A_{1/2}^+$
744 states responsible for spin-orbit predissociation. $\hat{\epsilon} \cdot \boldsymbol{\mu}$ is the dipole transition operator.

745 Expression (B1) can be simplified in several ways. First, we write the continuum wave
746 function as a partial-wave expansion³²,

$$\langle d\Omega\mathbf{k}| = \sum_{JM} (2J+1)^{1/2} i^J e^{-i\delta_J} D_{M\Omega}^J(\phi, \theta, 0) \langle dk\Omega JM|, \quad (\text{B2})$$

747 where ϕ, θ are the angles between the vectors $\hat{\epsilon}$ and \mathbf{k} , $D_{M\Omega}^J$ represents a Wigner rotation ma-
748 trix, and δ_J is the scattering phase shift. The total angular momentum quantum number J'
749 of the intermediate state and its projection quantum number M' are conserved upon predis-
750 sociation. Moreover, since predissociation is unaffected by the orientation of the molecular
751 ion in the lab-fixed frame, the corresponding matrix element should be independent of M' .
752 We combine these two properties by writing

$$\langle dk\Omega JM|H_v|e\Omega'J'M'\rangle = R_{e\Omega', dk\Omega}^{J'} \delta_{J'J} \delta_{M'M}. \quad (\text{B3})$$

753 In a second step, we assume that the broadening of the transition resulting from predisso-
754 ciation ($\Gamma_{eJ'}$ full width at half maximum) is significantly smaller than the energy spacing
755 between adjacent rotational levels, so that the rotational structure of the intermediate state

756 can be resolved. Therefore, when the photon energy is resonant with a transition, only the
757 term associated to this transition contributes significantly to the sum in Eq. (B1) and other
758 off-resonant terms can be neglected.

In a third step, we rewrite the squared norm of the transition dipole matrix element in terms of the transition line strength $S(iN''; eJ')$, giving

$$|\langle e\Omega' J' M' | \hat{\epsilon} \cdot \boldsymbol{\mu} | i\Lambda'' S'' N'' J'' M'' \rangle|^2 = \begin{pmatrix} J' & 1 & J'' \\ -M' & 0 & M'' \end{pmatrix}^2 S(i\Lambda'' S'' N'' J''; e\Omega' J') \quad (\text{B4})$$

in the case of linear polarization. Equation (B1) can now be rewritten as

$$\begin{aligned} \frac{d\sigma}{d\Omega} &= \frac{(2\pi)^2}{\hbar c} \frac{(2J' + 1) |R_{e\Omega' d\Omega}^{J'}|^2}{(E_{iN''} + \hbar\omega - E_{eJ'})^2 + \left(\frac{\Gamma_{eJ'}}{2}\right)^2} \\ &\times S(i\Lambda'' S'' N'' J''; e\Omega' J') \\ &\times \begin{pmatrix} J' & 1 & J'' \\ -M'' & 0 & M'' \end{pmatrix}^2 |D_{M''\Omega}^{J''}(\phi, \theta, 0)|^2, \end{aligned} \quad (\text{B5})$$

759 where we used the fact that $M' = M''$ for a dipole transition with linear polarization along
760 the z axis of the laboratory frame.

761 The total differential cross section is obtained by summing over the relevant initial and
762 final states. In the present case there are two dissociation continua with $\Omega = \pm 1/2$. We use
763 the fact that the squared norm of the Wigner D matrix in Eq. (B5) is independent of the
764 sign of Ω ⁶³. Moreover, Fermi's golden rule allows one to relate the predissociation matrix
765 element $R_{e\Omega' d\Omega}^{J'}$ to the predissociation rate $\Gamma_{eJ'}$,

$$\sum_{\Omega=-1/2}^{1/2} |R_{e\Omega' d\Omega}^{J'}|^2 = \frac{\Gamma_{eJ'}}{2\pi}. \quad (\text{B6})$$

Finally, we assume that all degenerate levels associated to the initial ground state are equally

populated. This leads to

$$\begin{aligned} \frac{d\sigma}{d\Omega} = & \frac{(2\pi)^2}{\hbar c} \frac{(2J' + 1)}{(2S'' + 1)(2N'' + 1)} \\ & \times \frac{1}{\pi} \frac{\frac{1}{2}\Gamma_{eJ'}}{(E_{iN''} + \hbar\omega - E_{eJ'})^2 + \left(\frac{\Gamma_{eJ'}}{2}\right)^2} \\ & \times \sum_{J''=|N''-S''|}^{N''+S''} S(i\Lambda''S''N''J''; e\Omega'J') \\ & \times \sum_{M''} \left(\begin{array}{ccc} J' & 1 & J'' \\ -M'' & 0 & M'' \end{array} \right)^2 \left| d_{M''|\Omega}^{J'}(\theta) \right|^2, \end{aligned} \quad (\text{B7})$$

766 where $d_{M''|\Omega}^{J'}$ is a small-d Wigner matrix. The sum over M'' on the right-hand side of the
767 above equation is known analytically and can be written as $\frac{1}{2}(1 + \beta_{J'J''}P_2(\cos\theta))$. The
768 corresponding formulas for $\beta_{J'J''}$ have been tabulated by Zare⁶⁴ (see also Pernot *et al.*⁵⁵).
769 Other terms on the right-hand side of Eq. (B7) include the ratio between the degeneracies of
770 the final and initial states, a Lorentzian function describing the transition line shape, and a
771 sum of the angular distribution of all degenerate J'' levels belonging to a given N'' , weighted
772 by the respective line strengths. Eq. (12) can be obtained from Eq. (B7).

773 Appendix C: Calculation of the Franck-Condon factors

774 The Franck-Condon factors f_{bb} of transitions between bound states presented in Fig.
775 10(c) were calculated in the usual way as

$$f_{\text{bb}} = \langle v' | v'' \rangle^2, \quad (\text{C1})$$

776 where $|v''\rangle$ and $|v'\rangle$ correspond to the vibrational wavefunctions of the initial and final
777 states, respectively, obtained by solving the nuclear Schrödinger equation. For transitions
778 to continuum states, we computed the Franck-Condon density⁶⁵

$$f \frac{df}{d\tilde{\nu}}(\tilde{\nu}) = \langle \tilde{\nu} | v'' \rangle^2, \quad (\text{C2})$$

779 where we label the energy-normalized continuum state $|\tilde{\nu}\rangle$ with the transition wave number
780 $\tilde{\nu}$. Although the expressions in Eqs. (C1) and (C2) are widely used to discuss transition
781 intensities, they do not allow for a direct comparison of transition probabilities to bound

782 states and to continuum states because of their different meaning. To obtain the Franck-
783 Condon factors of transitions to continuum states that are directly comparable with Eq.
784 (C1), we integrated the Franck-Condon density over the bandwidth of the laser radiation
785 responsible for photodissociation,

$$f_{bc}(\tilde{\nu}_L) = \frac{1}{\tilde{I}_0} \int \frac{df}{d\tilde{\nu}}(\tilde{\nu}) \tilde{I}(\tilde{\nu}) d\tilde{\nu}. \quad (\text{C3})$$

786 In Eq. (C3), $\tilde{I}(\tilde{\nu})$ is the laser spectral intensity distribution, \tilde{I}_0 is the maximum laser spectral
787 intensity, and $\tilde{\nu}_L$ the corresponding central wave number. Continuum Franck-Condon factors
788 f_{bc} thus depend on experimental conditions. Assuming that the laser spectral intensity is
789 well described by a Gaussian function and that the Franck-Condon density is approximately
790 constant over the laser bandwidth $\Delta\tilde{\nu}$, the integral can be approximated by

$$f_{bc}(\tilde{\nu}_L) \approx \frac{1}{\tilde{I}_0} \frac{df}{d\tilde{\nu}}(\tilde{\nu}_L) \int \tilde{I}(\tilde{\nu}) d\tilde{\nu} = \frac{\sqrt{\pi}\Delta\tilde{\nu}}{2\sqrt{\ln 2}} \frac{df}{d\tilde{\nu}}(\tilde{\nu}_L). \quad (\text{C4})$$

791 In our calculations we used exterior complex scaling (ECS)^{28,58} to compute the continuum
792 solutions of the nuclear Schrödinger equation. Within the framework of ECS, the Franck-
793 Condon density can be computed as⁶⁶

$$\frac{df}{d\tilde{\nu}}(\tilde{\nu}) = \frac{1}{\pi} \text{Im} \sum_{v_\theta} \frac{\langle v_\theta | v'' \rangle^2}{E_{v_\theta} - E_{v''} - hc\tilde{\nu}}, \quad (\text{C5})$$

794 which is a continuous function in $\tilde{\nu}$. In Eq. (C5), θ designates the complex-rotation angle,
795 $E_{v''}$ denotes the energy eigenvalue of the initial state, and E_{v_θ} is the complex energy eigen-
796 value of the continuum state $|v_\theta\rangle$. The Franck-Condon factors of the $B^+(v') \leftarrow X^+(v'' = 7)$
797 transitions were calculated using Eqs. (C1) and (C4) for the bound-bound (regions (i) and
798 (ii)) and the bound-continuum transitions (region (iii)), respectively. The Franck-Condon
799 factors $f_{2p}(\tilde{\nu}_{v'v''})$ of the resonant $\text{Mg}(3d)\text{Ar}^+ \ ^2\Sigma^+ \leftarrow B^+(v') \leftarrow X^+(v'' = 7)$ two-photon
800 transitions were calculated as products of the bound-bound Franck-Condon factor $\langle v' | v'' \rangle^2$
801 for the first excitation step and the bound-continuum Franck-Condon factor defined in Eq.
802 (C4) for the second, dissociative transition, i.e.,

$$f_{2p}(\tilde{\nu}_{v'v''}) = \langle v' | v'' \rangle^2 \cdot \frac{\sqrt{\pi}\Delta\tilde{\nu}}{2\sqrt{\ln 2}} \frac{df}{d\tilde{\nu}}(\tilde{\nu}_{v'v''}), \quad (\text{C6})$$

803 where $\Delta\tilde{\nu} = 0.1 \text{ cm}^{-1}$ in our experiment.

804 REFERENCES

- 805 ¹J. P. Maier, *Int. J. Mass Spectrom. Ion Processes* **104**, 1 (1991).
- 806 ²L. Zhu and P. Johnson, *J. Chem. Phys.* **94**, 5769 (1991).
- 807 ³K. Müller-Dethlefs and E. W. Schlag, *Angew. Chem. (int. ed. engl.)* **37**, 1346 (1998).
- 808 ⁴M. A. Duncan, *Int. J. Mass Spectrom.* **200**, 545 (2000).
- 809 ⁵T. Oka, in *The Encyclopedia of Mass Spectrometry*, Vol. 1 (Elsevier, Amsterdam, 2003) p.
810 217.
- 811 ⁶S. K. Stephenson and R. J. Saykally, *Chem. Rev.* **105**, 3220 (2005).
- 812 ⁷T. Amano, in *Handbook of High-Resolution Spectroscopy*, edited by M. Quack and F. Merkt
813 (John Wiley & Sons, Chichester, 2011) pp. 1267–1289.
- 814 ⁸S. Willitsch, in *Handbook of High-Resolution Spectroscopy*, edited by M. Quack and
815 F. Merkt (John Wiley & Sons, Chichester, 2011) pp. 1691–1712.
- 816 ⁹F. Merkt, S. Willitsch, and U. Hollenstein, in *Handbook of High-Resolution Spectroscopy*,
817 Vol. 3, edited by M. Quack and F. Merkt (John Wiley & Sons, Chichester, 2011) pp.
818 1617–1654.
- 819 ¹⁰S. Brünken, L. Kluge, A. Stoffels, J. Pérez-Ríos, and S. Schlemmer, *J. Mol. Spectrosc.*
820 **332**, 67 (2017).
- 821 ¹¹D. Schröder and H. Schwarz, *J. Phys. Chem. A* **103**, 7385 (1999).
- 822 ¹²R. S. Mulliken, *J. Am. Chem. Soc.* **86**, 3183 (1964).
- 823 ¹³I. Velchev, W. Hogervorst, and W. Ubachs, *J. Phys. B: At. Mol. Opt. Phys.* **32**, L511
824 (1999).
- 825 ¹⁴M. Génévriez, D. Wehrli, J. A. Agner, and F. Merkt, *Int. J. Mass Spectrom.* **435**, 209
826 (2019).
- 827 ¹⁵H. Partridge, C. W. Bauschlicher, and S. R. Langhoff, *J. Phys. Chem.* **96**, 5350 (1992).
- 828 ¹⁶R. J. Le Roy, *J. Chem. Phys.* **101**, 10217 (1994).
- 829 ¹⁷C. W. Bauschlicher Jr. and H. Partridge, *Chem. Phys. Lett.* **239**, 241 (1995).
- 830 ¹⁸K. L. Burns, D. Bellert, A. W. Leung, and W. H. Breckenridge, *J. Chem. Phys.* **114**, 7877
831 (2001).
- 832 ¹⁹D. Bellert and W. H. Breckenridge, *Chem. Rev.* **102**, 1595 (2002).
- 833 ²⁰A. M. Gardner, C. D. Withers, J. B. Graneek, T. G. Wright, L. A. Viehland, and W. H.
834 Breckenridge, *J. Phys. Chem. A* **114**, 7631 (2010).

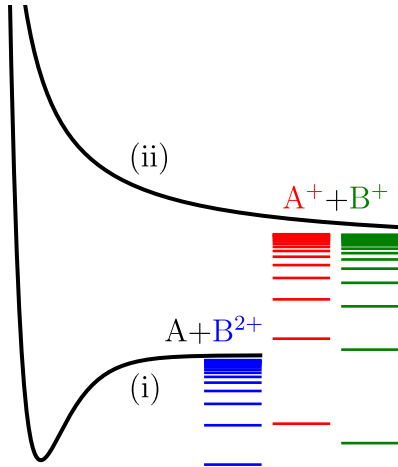
- 835 ²¹W. Gaied, H. Habli, B. Oujia, and F. X. Gadea, *Eur. Phys. J. D* **62**, 371 (2011).
- 836 ²²W. D. Tuttle, J. P. Harris, Y. Zheng, W. H. Breckenridge, and T. G. Wright, *J. Phys.*
837 *Chem. A* **122**, 7679 (2018).
- 838 ²³J. S. Pilgrim, C. S. Yeh, and M. A. Duncan, *Chem. Phys. Lett.* **210**, 322 (1993).
- 839 ²⁴J. S. Pilgrim, C. S. Yeh, K. R. Berry, and M. A. Duncan, *J. Chem. Phys.* **100**, 7945
840 (1994).
- 841 ²⁵C. S. Yeh, J. S. Pilgrim, K. F. Willey, D. L. Robbins, and M. A. Duncan, *Int. Rev. Phys.*
842 *Chem.* **13**, 231 (1994).
- 843 ²⁶C. T. Scurlock, J. S. Pilgrim, and M. A. Duncan, *J. Chem. Phys.* **103**, 3293 (1995).
- 844 ²⁷M. Génévriez, D. Wehrli, and F. Merkt, *Mol. Phys.* **118**, e1703051 (2020).
- 845 ²⁸M. Génévriez, D. Wehrli, and F. Merkt, (2020), submitted, companion article.
- 846 ²⁹D. Wehrli, M. Génévriez, C. Kreis, J. A. Agner, and F. Merkt, *J. Phys. Chem. A* **124**,
847 379 (2020).
- 848 ³⁰R. R. Bennett, J. G. McCaffrey, and W. H. Breckenridge, *J. Chem. Phys.* **92**, 2740 (1990).
- 849 ³¹R. R. Bennett, J. G. McCaffrey, I. Wallace, D. J. Funk, A. Kowalski, and W. H. Breck-
850 enridge, *J. Chem. Phys.* **90**, 2139 (1989).
- 851 ³²R. N. Zare, *Mol. Photochem.* **4**, 1 (1972).
- 852 ³³R. N. Dixon, *J. Chem. Phys.* **122**, 194302 (2005).
- 853 ³⁴A. Shee, T. Saue, L. Visscher, and A. Severo Pereira Gomes, *J. Chem. Phys.* **149**, 174113
854 (2018).
- 855 ³⁵T. Fleig, J. Olsen, and L. Visscher, *J. Chem. Phys.* **119**, 2963 (2003).
- 856 ³⁶S. Knecht, H. J. Aa. Jensen, and T. Fleig, *J. Chem. Phys.* **132**, 014108 (2010).
- 857 ³⁷S. Knecht, Ö. Legeza, and M. Reiher, *J. Chem. Phys.* **140**, 041101 (2014).
- 858 ³⁸S. Battaglia, S. Keller, and S. Knecht, *J. Chem. Theory Comput.* **14**, 2353 (2018).
- 859 ³⁹T. H. Dunning Jr., *J. Chem. Phys.* **90**, 1007 (1989).
- 860 ⁴⁰J. Thyssen, *Development and Applications of Methods for Correlated Relativistic Calcula-*
861 *tions of Molecular Properties*, Dissertation, Department of Chemistry, University of South-
862 ern Denmark (2001).
- 863 ⁴¹J. Sikkema, L. Visscher, T. Saue, and M. Iliaš, *J. Chem. Phys.* **131**, 124116 (2009).
- 864 ⁴²DIRAC, a relativistic ab initio electronic structure program, Release DIRAC19 (2019),
865 written by A. S. P. Gomes, T. Saue, L. Visscher, H. J. Aa. Jensen, and R. Bast, with
866 contributions from I. A. Aucar, V. Bakken, K. G. Dyall, S. Dubillard, U. Ekström,

- 867 E. Eliav, T. Enevoldsen, E. Faßhauer, T. Fleig, O. Fossgaard, L. Halbert, E. D. Hedegård,
868 B. Heimlich–Paris, T. Helgaker, J. Henriksson, M. Iliáš, Ch. R. Jacob, S. Knecht, S. Ko-
869 morovský, O. Kullie, J. K. Lærdahl, C. V. Larsen, Y. S. Lee, H. S. Nataraj, M. K. Nayak,
870 P. Norman, G. Olejniczak, J. Olsen, J. M. H. Olsen, Y. C. Park, J. K. Pedersen, M. Pern-
871 pointner, R. di Remigio, K. Ruud, P. Salek, B. Schimmelpfennig, B. Senjean, A. Shee,
872 J. Sikkema, A. J. Thorvaldsen, J. Thyssen, J. van Stralen, M. L. Vidal, S. Villaume,
873 O. Visser, T. Winther, and S. Yamamoto (available at [http://dx.doi.org/10.5281/](http://dx.doi.org/10.5281/zenodo.3572669)
874 [zenodo.3572669](http://dx.doi.org/10.5281/zenodo.3572669), see also <http://www.diracprogram.org>).
- 875 ⁴³T. Saue, R. Bast, A. S. P. Gomes, H. J. Aa. Jensen, L. Visscher, I. A. Aucar, R. di Remigio,
876 K. G. Dyall, E. Eliav, E. Faßhauer, T. Fleig, L. Halbert, E. D. Hedegård, B. Heimlich-Paris,
877 M. Iliáš, C. R. Jacob, S. Knecht, J. K. Lærdahl, M. L. Vidal, M. K. Nayak, G. Olejniczak,
878 J. M. H. Olsen, M. Pernpointner, B. Senjean, A. Shee, A. Sunaga, and J. van Stralen, J.
879 Chem. Phys. **152**, 204104 (2020).
- 880 ⁴⁴S. Keller, M. Dolfi, M. Troyer, and M. Reiher, J. Chem. Phys. **143**, 244118 (2015).
- 881 ⁴⁵S. Knecht, E. D. Hedegaard, S. Keller, A. Kovyrshin, Y. Ma, A. Muolo, C. J. Stein, and
882 M. Reiher, Chimia **70**, 244 (2016).
- 883 ⁴⁶A. Kramida, Yu. Ralchenko, J. Reader, and NIST ASD Team, NIST Atomic Spectra
884 Database (ver. 5.6.1), [Online]. Available: <https://physics.nist.gov/asd> [2020, May
885 25]. National Institute of Standards and Technology, Gaithersburg, MD. (2019).
- 886 ⁴⁷K. A. Peterson and T. H. Dunning, Jr., J. Chem. Phys. **117**, 10548 (2002).
- 887 ⁴⁸B. P. Prascher, D. E. Woon, K. A. Peterson, T. H. Dunning, Jr., and A. K. Wilson, Theor.
888 Chem. Acc. **128**, 69 (2011).
- 889 ⁴⁹J. S. Pilgrim, C. S. Yeh, K. R. Berry, and M. A. Duncan, J. Chem. Phys. **100**, 7945
890 (1994).
- 891 ⁵⁰The wave numbers of the $X^+ 2\Sigma^+(v'' = 7) \leftarrow a^3\Pi_0(v = 0)$ ionizing transitions of ²⁴MgAr,
892 ²⁵MgAr, and ²⁶MgAr reported in Table 1 (third column) of Ref. 29 must be corrected from
893 39341.1(5) cm⁻¹, 39334.7(5) cm⁻¹, and 39328.8(5) cm⁻¹, respectively, to 39340.5(5) cm⁻¹,
894 39334.1(5) cm⁻¹, and 39328.2(5) cm⁻¹. All other table entries are not affected.
- 895 ⁵¹G. Herzberg, *Molecular Spectra and Molecular Structure, Volume I, Spectra of Diatomic*
896 *Molecules*, 2nd ed. (Van Nostrand Reinhold Company, New York, 1950).
- 897 ⁵²J. Thijssen, *Computational Physics*, 2nd ed. (Cambridge University Press, 2007).
- 898 ⁵³H. Hoshino, Y. Yamakita, K. Okutsu, Y. Suzuki, M. Saito, K. Koyasu, K. Ohshimo, and

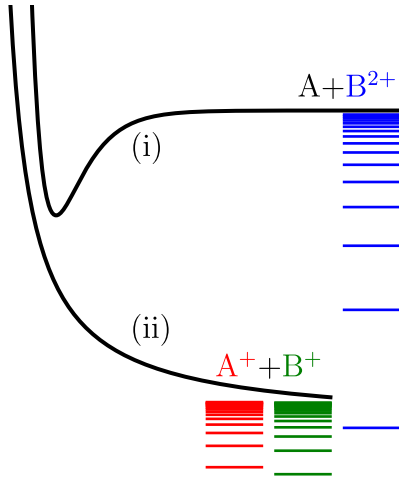
This is the author's peer reviewed, accepted manuscript. However, the online version of record will be different from this version once it has been copyedited and typeset.
PLEASE CITE THIS ARTICLE AS DOI:10.1063/1.5015603

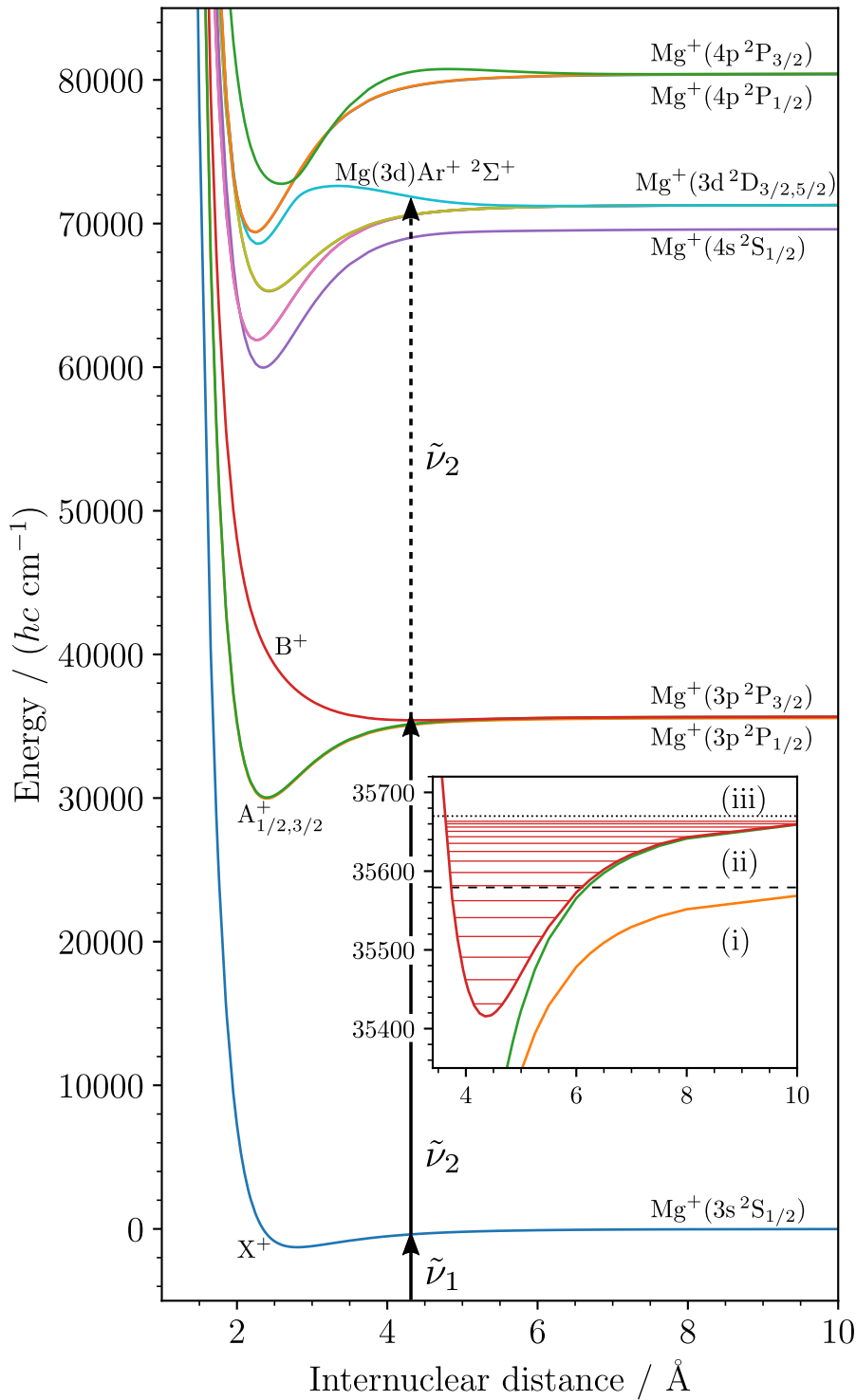
- 899 F. Misaizu, Chem. Phys. Lett. **630**, 111 (2015).
900 ⁵⁴C. Jonah, J. Chem. Phys. **55**, 1915 (1971).
901 ⁵⁵C. Pernot, J. Durup, J. Ozenne, J. A. Beswick, P. C. Cosby, and J. T. Moseley, J. Chem.
902 Phys. **71**, 2387 (1979).
903 ⁵⁶R. N. Zare, *Angular Momentum* (John Wiley & Sons, New York, 1988).
904 ⁵⁷D. Manolopoulos and R. Wyatt, Chem. Phys. Lett. **152**, 23 (1988).
905 ⁵⁸T. N. Rescigno and C. W. McCurdy, Phys. Rev. A **62**, 032706 (2000).
906 ⁵⁹D. A. Telnov and S. Chu, Phys. Rev. A **59**, 2864 (1999).
907 ⁶⁰S. Mukamel and J. Jortner, J. Chem. Phys. **61**, 5348 (1974).
908 ⁶¹B. R. Cosofret, H. M. Lambert, and P. L. Houston, J. Chem. Phys. **117**, 8787 (2002).
909 ⁶²H. Kim, K. S. Dooley, S. W. North, G. E. Hall, and P. L. Houston, J. Chem. Phys. **125**
910 (2006), 10.1063/1.2216708.
911 ⁶³D. A. Varshalovich, A. N. Moskalev, and V. K. Khersonskii, in *Quantum Theory of*
912 *Angular Momentum* (World Scientific, 1988) pp. 72–129.
913 ⁶⁴R. N. Zare, J. Chem. Phys. **40**, 1934 (1964).
914 ⁶⁵J. Tellinghuisen, in *Photodissociation and Photoionization*, Advances in Chemical Physics,
915 Vol. LX, edited by K. P. Lawley (John Wiley Sons, 1985) pp. 299–369.
916 ⁶⁶T. N. Rescigno and V. McKoy, Phys. Rev. A **15**, 522 (1975).

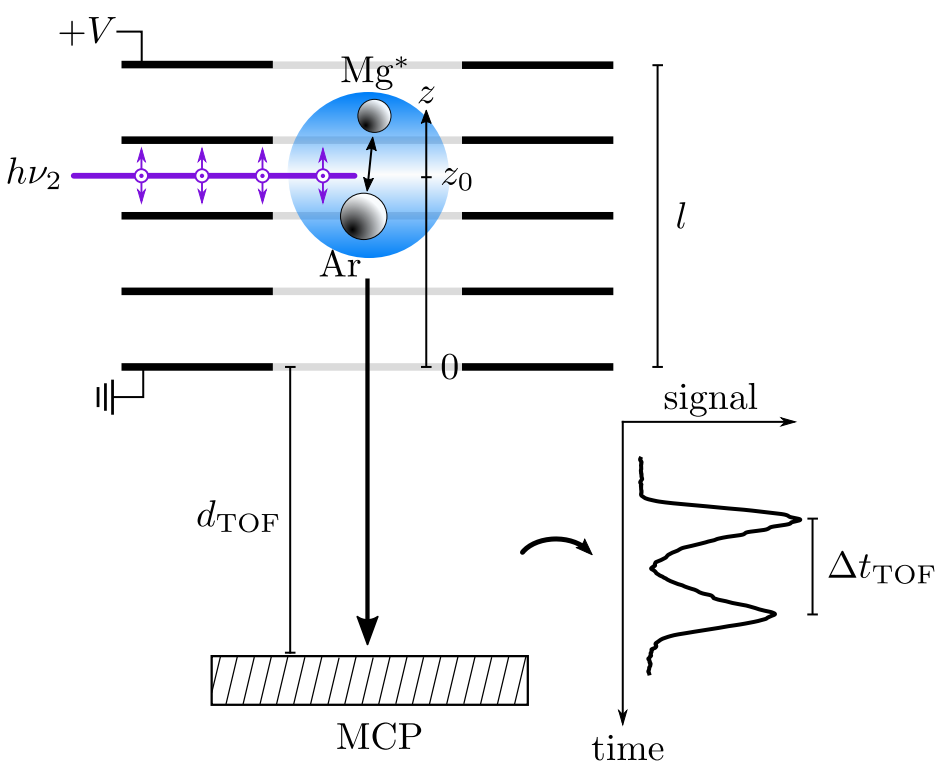
(a)

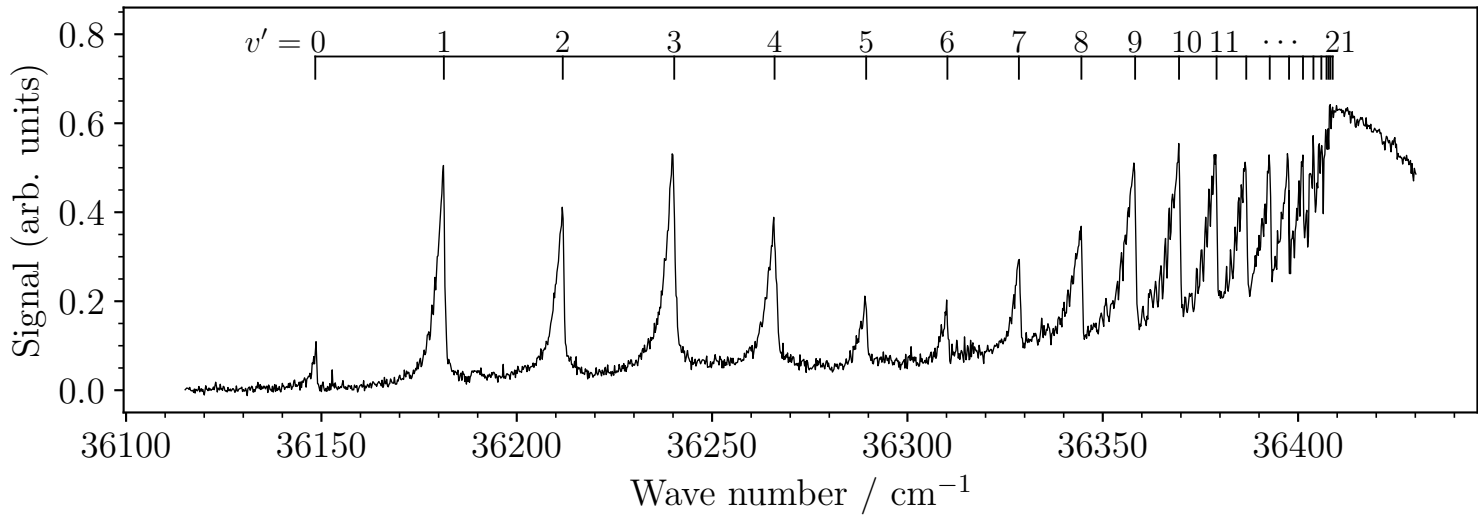


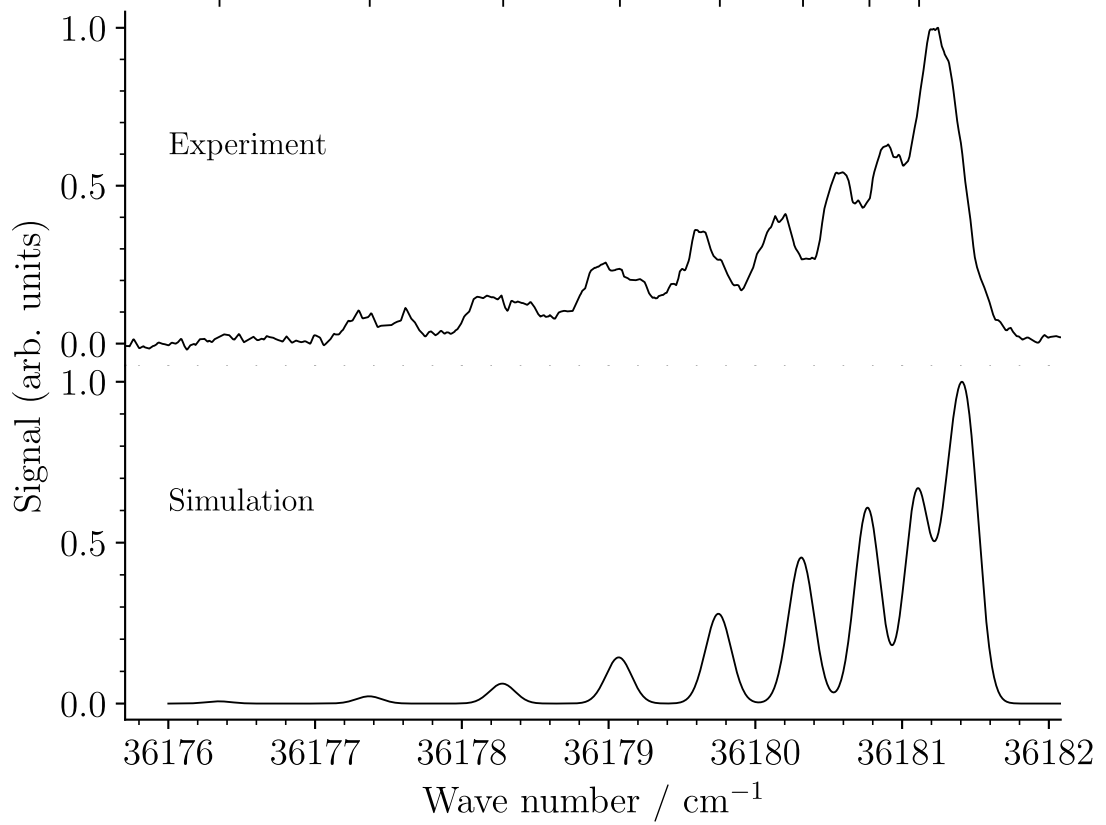
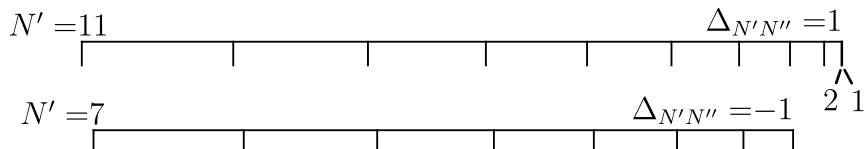
(b)

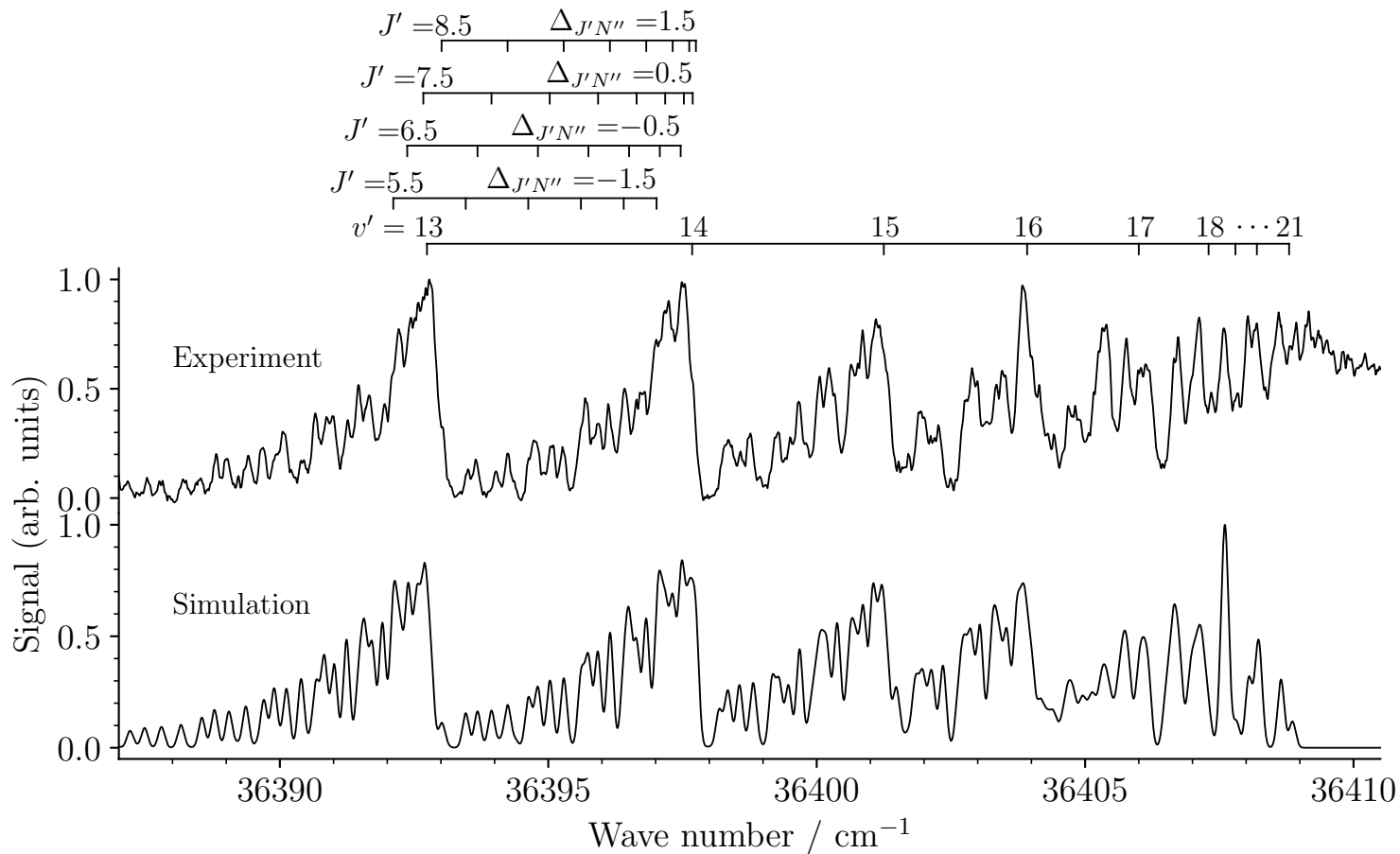




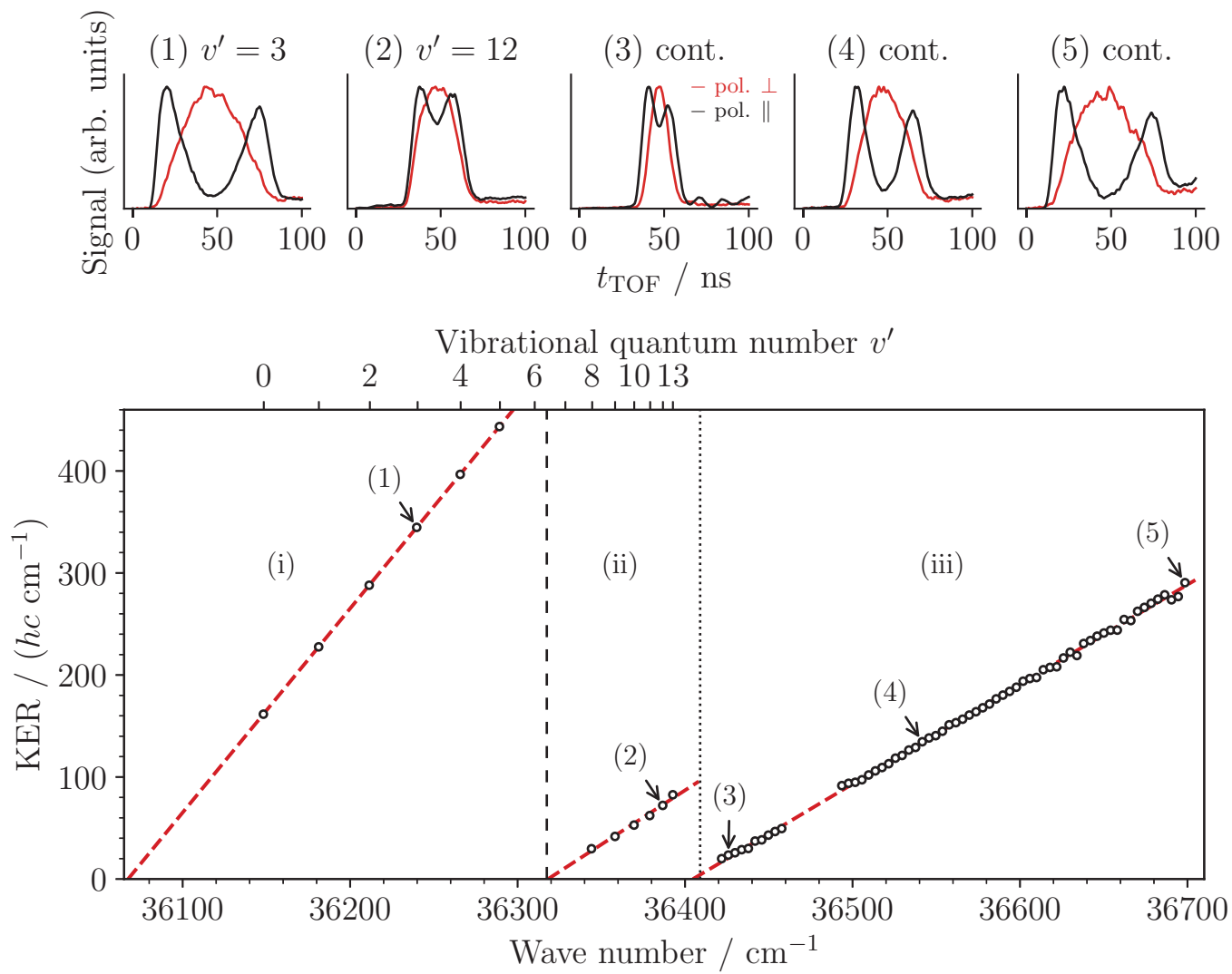


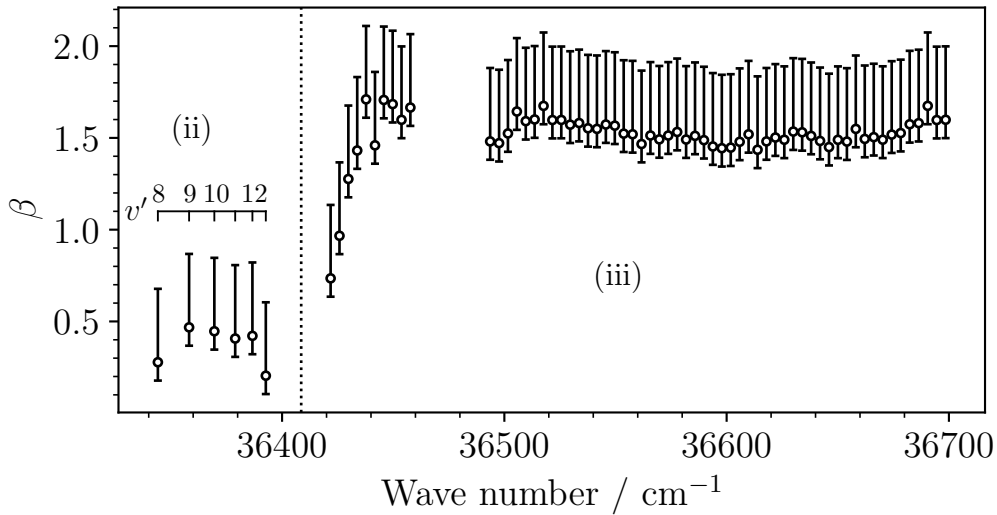




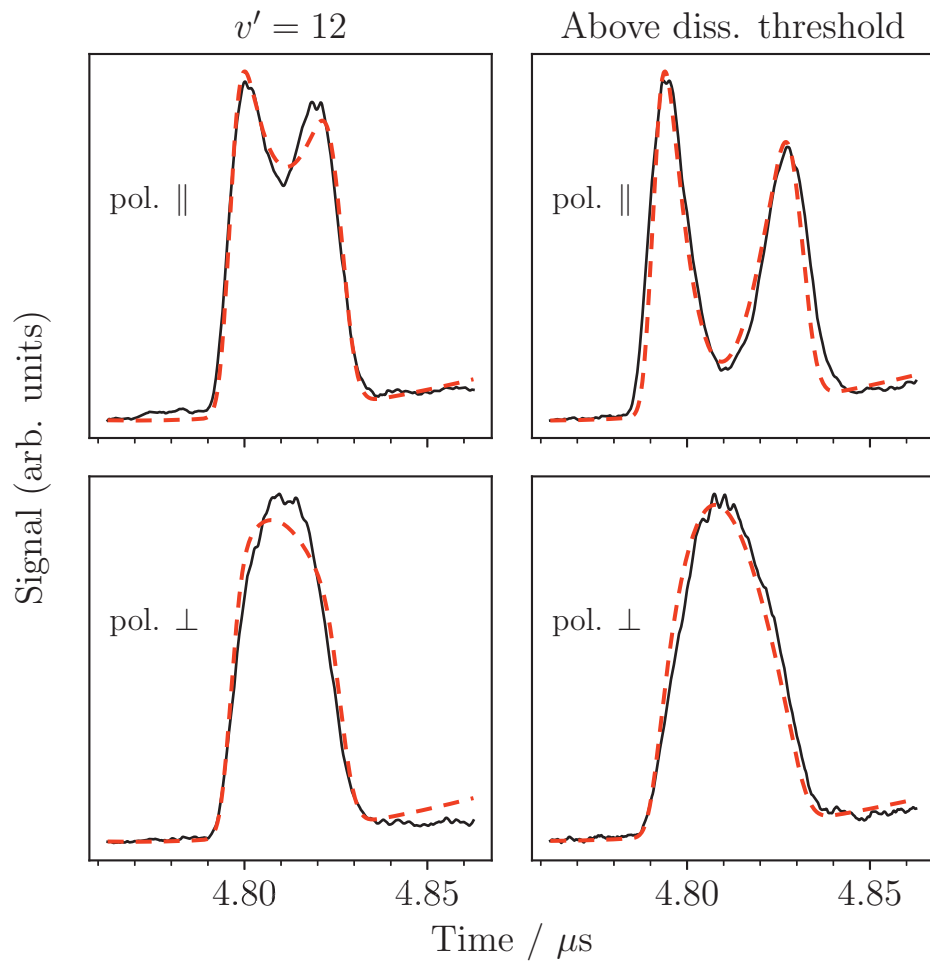


This is the author's peer reviewed, accepted manuscript. However, the online version of record will be different from this version once it has been copyedited and typeset.
PLEASE CITE THIS ARTICLE AS DOI:10.1063/1.5015603





This is the author's peer reviewed, accepted manuscript. However, the online version of record will be different from this version once it has been copyedited and typeset.
PLEASE CITE THIS ARTICLE AS DOI:10.1063/1.50015603



This is the author's peer reviewed, accepted manuscript. However, the online version of record will be different from this version once it has been copyedited and typeset.
PLEASE CITE THIS ARTICLE AS DOI:10.1063/1.50015603

